

Comparison of ocean vertical mixing schemes in the Max Planck Institute Earth System Model (MPI-ESM1.2)

Oliver Gutjahr¹, Nils Brüggemann^{1,2}, Helmuth Haak¹, Johann H. Jungclaus¹, Dian A. Putrasahan¹, Katja Lohmann¹, and Jin-Song von Storch^{1,3}

¹Max Planck Institute for Meteorology, Hamburg, Germany

²University of Hamburg, Hamburg, Germany

³Center for Earth System Research and Sustainability (CEN), University of Hamburg, Germany

Correspondence: O. Gutjahr (oliver.gutjahr@mpimet.mpg.de)

Abstract. We compare the effects of four different ocean vertical mixing schemes on the mean state of the ocean and atmosphere in the Max Planck Institute Earth System Model (MPI-ESM1.2). Besides the default Pacanowski and Philander (1981) (PP) scheme, we use the K-profile parameterisation (KPP) from the Community Vertical Mixing (CVMix) library and have implemented a scheme based on turbulent kinetic energy (TKE) and a recently developed prognostic scheme for internal wave energy and its dissipation (IDEMIX) to replace the often assumed constant background diffusivity in the ocean interior. We analyse in particular the effects of IDEMIX on the ocean mean state, when combined with TKE (TKE+IDEMIX).

We find warmer sea surface temperatures (SSTs) in the North Atlantic and Nordic Seas using KPP or TKE(+IDEMIX), which is related to 10 % higher overflows that cause a stronger and deeper upper cell of the Atlantic meridional overturning circulation (AMOC) and thereby an enhanced northward heat transport and higher inflow of warm and saline water from the Indian Ocean into the South Atlantic. A saltier subpolar North Atlantic and Nordic Seas leads to increased deep convection and thus to the increased overflows. Due to the warmer SSTs, the extratropics of the northern hemisphere become warmer with TKE(+IDEMIX), weakening the meridional gradient and thus the jet stream. With KPP, the tropics and the southern hemisphere also become warmer without weakening the jet stream. Using an energetically more consistent scheme (TKE+IDEMIX) produces a more heterogeneous and realistic pattern of vertical eddy diffusivity, with lower diffusivities in deep and flat-bottom basins and elevated turbulence over rough topography. IDEMIX improves in particular the diffusivity in the Arctic Ocean and reduces the warm bias in the Atlantic water layer. We conclude that although shortcomings due to model resolution determine the global-scale bias pattern, the choice of the vertical mixing scheme may play an important role for regional biases.

Copyright statement. TEXT

1 Introduction

Vertical mixing in the ocean is a complex phenomena and its magnitude depends on processes acting over a large range of vertical and horizontal scales, from about 1 km to several meters down to centimetres (Fox-Kemper et al., 2019). Vertical mixing

affects key elements in the ocean that are of climatic importance, such as ocean stratification, the distribution of temperature, salinity and passive tracers, the ocean uptake of heat and carbon, and the global meridional overturning circulation (MOC; e.g. Gent, 2018).

25 In ocean models, the processes that lead to mixing are subgrid-scale and therefore not resolved, so they have to be parameterised. The complexity of these parameterisations varies in dependence of our understanding, application, and available resources (e.g. Large et al., 1994; Fox-Kemper et al., 2019). In fact, the parameterisation of vertical mixing constitutes one of the current shortcomings of ocean models (Robertson and Dong, 2019; Fox-Kemper et al., 2019).

We compare four ocean vertical mixing schemes in coupled simulations with the Max Planck Institute Earth System Model
30 (MPI-ESM1.2). Such a comparison provides a better understanding of the model behaviour at the process level, especially when the same model is used. It is therefore very helpful to have libraries that provide different choices for parameterisations, such as the Community Vertical Mixing (CVMix) library (Griffies et al., 2015; Van Roekel et al., 2018). We have coupled CVMix to MPI-ESM1.2 and used its infrastructure to extend the library by the turbulent kinetic energy (TKE) scheme (Gaspar et al., 1990) and a prognostic scheme for internal wave energy in the ocean, called Internal Wave Dissipation, Energy and
35 Mixing (IDEMIX; Olbers and Eden, 2013), which are not yet an official part of CVMix (see section 2 and appendix A3).

Frequently used ocean vertical mixing schemes date back to the 1980s and 1990s. Often a modelling centre or a group decides to implement only one of these schemes and, for practical reasons such as tuning effort, not to deviate from it afterwards. However, as these schemes are based on different principles, deviations in the results are to be expected. We further note that even the same scheme may produce different results due to the numerical implementation (e.g. Li et al., 2019) and small
40 modifications (e.g. Danabasoglu et al., 2006).

In the ocean surface boundary layer, schemes diagnose vertical profiles of scalar mixing diffusivity and viscosity from surface forcing and background fields, such as in the PP scheme (Pacanowski and Philander, 1981) or in the K-profile parameterisation (KPP; Large et al., 1994). Second order schemes (Mellor and Yamada, 1982), such as the TKE scheme (Gaspar et al., 1990), contain in addition to the mean quantities also prediction equations for higher order moments, i.e. for variance and covariance
45 terms of heat and momentum. These two most common approaches represent processes that result in vertical shear of the velocity and in changes of the buoyancy, e.g. due to convection. These schemes can become more complex by adding further sub-grid scale processes (Fox-Kemper et al., 2019), such as mixing by Langmuir turbulence (e.g. McWilliams et al., 1997; Li and Fox-Kemper, 2017; Li et al., 2019) or internal tides (Garrett, 2003). Although KPP is probably the most widely used scheme in ocean models, TKE is also a frequent choice and is part of state-of-the-art ocean models, and for which also extensions such
50 as Langmuir turbulence (Axell, 2002) or surface waves (Breivik et al., 2015) were developed.

The remainder of the manuscript is organized as follows. We first give a brief overview of the model configuration in section 2, with more details about the vertical mixing schemes and the experiments we conducted. In section 3, we present the results of the comparison for the global ocean and in section 4 for the regional ocean. Section 5 presents effects of the mixing scheme in the atmosphere. Finally, we conclude in section 6.

55 2 Model configuration

For our analysis we used the Max Planck Institute Earth System Model in version 1.2.01 (MPI-ESM1.2; Mauritsen et al., 2019) that was also used for the Coupled Model Intercomparison Project Phase 6 (CMIP6). The model consists of the atmospheric submodel ECHAM6.3 (Stevens et al., 2013), including the land-surface submodel JSBACH3.2, and of the ice-ocean submodel MPIOM1.6.3 (Jungclaus et al., 2013; Notz et al., 2013). The submodels are coupled via the Ocean-Atmosphere-Sea-Ice coupler
60 version 3 (OASIS3-mct; Valcke, 2013) with a coupling frequency of 1 h.

The horizontal resolution of the atmosphere is T127 (about 103 km) with 95 vertical levels. The ocean is discretised on a tripolar grid with a horizontal resolution of 0.4° (TP04; about 44 km) and 40 vertical levels, of which the first 20 levels are distributed in the top 750 m. A partial grid cell formulation (Adcroft et al., 1997; Wolff et al., 1997) was used to better represent the bottom topography. River runoff is calculated by a horizontal discharge model (Hagemann and Gates, 2003). Tracer
65 advection by unresolved mesoscale eddies is parameterised following Gent et al. (1995) (GM) with a constant eddy thickness diffusivity of $250\text{m}^2\text{s}^{-1}$ for a 400 km wide grid cell, which reduces linearly with increasing resolution (about $25\text{m}^2\text{s}^{-1}$ for a resolution of 40 km). The lateral eddy diffusivity is parameterised by an isopycnal formulation (Redi, 1982) with a constant value of $1000\text{m}^2\text{s}^{-1}$ for a 400 km wide grid cell, which again reduces linearly with increasing resolution (about $100\text{m}^2\text{s}^{-1}$ for a resolution of 40 km). The default parameterisation of ocean vertical mixing is a modified version PP scheme that was
70 extended with a wind-induced mixing term (Marsland et al., 2003). This model configuration is referred to as "high resolution" (HR) and was described and tested in more detail by Mauritsen et al. (2019), Müller et al. (2018), and Gutjahr et al. (2019).

To analyse the effect of different ocean vertical mixing schemes on the mean state, we coupled the CVMix library (Griffies et al., 2015; Van Roekel et al., 2018) to MPI-ESM1.2. KPP, as described in Large et al. (1994), is already included in CVMix and has been used with MPI-ESM1.2 by Gutjahr et al. (2019). In addition, we have added the TKE scheme (Gaspar et al., 1990;
75 Eden et al., 2014) and IDEMIX (Olbers and Eden, 2013) to CVMix, which is however not yet officially available. Although it is principally possible to couple IDEMIX to other mixing schemes, such as KPP, we only combined it with TKE because TKE and IDEMIX both rely on energy budgets, which results in a more consistent mixing scheme. In the following, we describe the ocean vertical mixing schemes in more detail. A complete description is given in appendix A.

2.1 Ocean vertical mixing schemes in MPI-ESM1.2

80 The default vertical mixing scheme in MPI-ESM1.2 is a modified version of the PP scheme that was extended with an additional wind-induced mixing term (Marsland et al., 2003). The modified PP scheme was used to tune MPI-ESM1.2 (Mauritsen et al., 2012), which is why we did not use the version that comes with CVMix. Recent experiments with a higher-resolution (T255 or ~ 50 km) version of ECHAM6.3, the atmospheric model developed at MPI-M, resulted in a collapse of the Atlantic meridional overturning circulation (AMOC) and icing of the Labrador Sea (Putrasahan et al., 2019). By replacing PP with KPP,
85 however, Gutjahr et al. (2019) showed that a stable AMOC is maintained. Complementing to the MPI-ESM1.2-HR simulations performed by Gutjahr et al. (2019) with PP and KPP, we perform two additional sensitivity experiments in which we replace the PP scheme by TKE (Gaspar et al., 1990), which has two alternatives for parameterising the background diffusivity.

The background diffusivity, which quantifies the mixing due to internal wave breaking, is either parameterised as a constant value (PP or KPP), or it depends on the buoyancy frequency and an artificial minimum value for the TKE scheme. We have implemented the TKE scheme with two alternatives for the background diffusivity. In the first case, we use a minimum value for TKE that is modified by the buoyancy frequency to represent the breaking of internal waves. In the second case, we do not assume an artificial minimum value for TKE, but combine the TKE scheme with IDEMIX, which describes the energy transfer from internal wave sources to wave sinks prognostically via a radiative transfer equation of weakly interacting internal waves (Olbers and Eden, 2013). Energy dissipated by internal waves (wave breaking) is treated as an energy source for TKE, resulting in a more energetically consistent solution. (Eden et al., 2014).

Furthermore, IDEMIX solves the propagation of low-mode waves away from their generation site (Fox-Kemper et al., 2019), in the vertical and horizontal (see appendix section A3 and Fig. A1), along with the energy loss the waves experience as they encounter different ocean regions and continental shelves. As the internal waves propagate, wave-wave interaction is accounted for that might dampen the waves (Olbers and Eden, 2013). Compared to empirical tidal mixing schemes, e.g. Simmons et al. (2004), IDEMIX represents not only internal waves generated by barotropic tides that interact with rough submarine topography, but also internal waves excited at the base of the mixed layer due to high-frequency wind fluctuations. Furthermore, in contrast to the tidal mixing scheme of Simmons et al. (2004), internal wave energy also propagates horizontally and might thus affect mixing at considerable distance from its generation site.

IDEMIX has been developed recently and its performance was studied in both stand-alone ocean models (Eden et al., 2014; Pollmann et al., 2017; Nielsen et al., 2018) and coupled simulations (Nielsen et al., 2018, 2019). Based on ocean-only simulations, the TKE dissipation calculated with a combined TKE and IDEMIX scheme agrees well with Argo float-derived dissipation rates (Pollmann et al., 2017). Using IDEMIX in coupled simulations, Nielsen et al. (2018) report only a minor effect on the sea surface temperature. However, they demonstrate reduced thermocline diffusivities with IDEMIX, which leads to a sharper and shallower thermocline, because less heat is mixed downwards. Although IDEMIX produces colder temperature within the first 1000 m of their simulations, at mid-depth the temperatures are in better agreement with observations.

Due to these promising results, we compare the effect of IDEMIX with the other mixing schemes of MPI-ESM1.2 and analyse regions that are most sensitive to IDEMIX on the typical time scale of 100 years for climate simulations.

2.2 Experiments

We performed four 100-year long simulations with MPI-ESM1.2-HR using four different ocean vertical mixing schemes. See Tab. 1 for an overview of the experiments and Appendix A for details of the mixing schemes.

The reference simulation (HR_{pp}) uses the PP scheme and exactly the configuration used by Müller et al. (2018) and Gutjahr et al. (2019). In the second simulation we used the KPP scheme and refer to it as HR_{kpp} . The configuration of this experiment is exactly as in Gutjahr et al. (2019). These two simulations were also compared with higher resolution versions (atmosphere and ocean) by Gutjahr et al. (2019), as part of the High-Resolution Model Intercomparison Project (HighResMIP; Haarsma et al., 2016).

The third experiment (HR_{tke}) used the TKE scheme with a background diffusivity that depends on the buoyancy frequency and on a minimum value for TKE (see Appendix A3), but without any contribution from IDEMIX. In the last experiment (HR_{ide}), we used the TKE scheme together with IDEMIX (TKE+IDEMIX) and replaced the artificial background diffusivity with one diagnosed from TKE that is fueled by the internal wave dissipation (see section A3 for more details). If not explicitly
125 mentioned, we used default values for the parameters of the mixing schemes, as listed in the respective original description (see also Appendix A), without analysing the effect of changed parameters.

The initial state was derived from a MPI-ESM1.2-HR simulation (with the PP scheme) that was nudged to the averaged temperature and salinity state of 1950 to 1954 of the Met Office Hadley Centre EN4 observational data set (version 4.2.0; Good et al. (2013)), as described in Gutjahr et al. (2019). All simulations were forced by constant 1950s conditions according
130 to the HighResMIP protocol (Haarsma et al., 2016). As recommended in this protocol, the model was not retuned to obtain isolated effects from changing the ocean vertical mixing scheme. If not stated otherwise, we analysed averages over the last 20 model years (model years 81 to 100). Although our focus is on the ocean, we briefly present results for the atmosphere as well.

3 Effects on the global ocean

In the following, we present how the choice of the ocean vertical mixing scheme affects the ocean mean state in control
135 simulations with MPI-ESM1.2-HR. We first present results for the global ocean, before discussing specific regional aspects in section 4.

3.1 Spatial distribution of vertical diffusivity

Away from boundary currents, deep convection areas and the surface mixed layer, the vertical diffusivity K is approximately
140 homogeneously distributed to leading order in the simulations with PP and KPP, which both use the simple constant background diffusivity of $K = 1.05 \cdot 10^{-5} \text{ m}^2 \text{ s}^{-2}$ for parameterising internal wave breaking, as demonstrated exemplarily for a model layer at intermediate depth of 1020 m (Fig. 1). Because of the relationship $K = \sqrt{2}E_{\text{min}}/N$ for the background diffusivity in the TKE scheme (see Appendix A3), HR_{tke} simulates a small K in the tropical and subtropical ocean, where N is positive and a large K in the high-latitude ocean, where N is negative. Even more heterogeneous is the distribution of K in HR_{ide} , which
145 simulates stronger mixing above rough topography and mixing coefficients of about two orders of magnitude lower above the abyssal plains and in the Arctic Ocean. Hotspots of strong vertical mixing are simulated for all four cases particularly in the subpolar North Atlantic (SPNA), in the Nordic Seas, and in the Weddell and Ross Sea of the Southern Ocean. Excessive deep convection in the Weddell Sea is a known issue in ocean models (e.g. Sallée et al., 2013; Kjellsson et al., 2015; Heuzé et al., 2015; Naughten et al., 2018) and not unique to MPI-ESM1.2-HR. The unrealistic convection is related to anomalously frequent open-ocean Weddell Sea polynyas (Gordon, 1978; Carsey, 1980; Gordon, 2014). HR_{ide} reduces the occurrence of this spurious
150 deep convection, which we will discuss in section 4.4.

A closer look at Fig. 1 reveals more regional differences in the above-mentioned areas. We will relate them to biases in temperature and salinity (section 3.2 and 3.4) and discuss them in more detail for the SPNA and Nordic Seas (section 4.1), the Fram Strait (section 4.2), the Arctic Ocean (section 4.3), and the Southern Ocean (section 4.4).

3.2 Sea surface temperature and salinity bias

155 The sea surface temperature (SST) is a key quantity for the atmosphere-ocean coupling. Reducing biases of SST in model simulations is thus of crucial importance. However, the causes of SST biases are often complex and result, among others, from insufficient horizontal and vertical resolution and from the need to parameterise subgrid-scale processes, which has the largest influence on the biases (Fox-Kemper et al., 2019). Vertical mixing is thereby only one of these parameterisations.

Overall, the SSTs are mostly colder in the MPI-ESM1.2-HR simulations compared with EN4 (Fig. 2). Although vertical
160 mixing has little effect on the SST bias in large parts of the ocean, some areas are more sensitive. One such area is the North Atlantic with its subpolar gyre, as well as the Nordic Seas. The largest cold bias occurs in the North Atlantic and amounts to -7°C in HR_{pp} . This cold bias is a common phenomena in ocean models (e.g. Randall et al., 2007) and is mainly caused by a too zonal pathway of the Gulf Stream (Dengg et al., 1996) in relation to insufficient horizontal resolution and northward heat transport (Wang et al., 2014). By using a vertical mixing scheme other than PP, we find that the SST cold bias in the
165 North Atlantic is reduced (Fig. 2b-d). This reduction of the cold bias can be explained by a generally warmer North Atlantic. A stronger Atlantic meridional overturning circulation (AMOC) in the simulations with KPP and TKE (see section 3.5) transports more heat northwards that leads to warmer temperatures in the SPNA, especially in the Labrador and Irminger Seas, and in the Nordic Seas.

Strong warm biases occur also in the tropical upwelling regions off the west coasts of Africa and South America, which is
170 related to insufficiently resolved coastal winds that force the upwelling of colder water (Milinski et al., 2016).

The sea surface salinity is mostly unaffected by the chosen vertical mixing scheme, except in the Arctic Ocean (Fig. 3). By using the TKE or TKE+IDEMIX scheme, the salinity bias is considerably reduced, especially in the Canada Basin (Fig. 3c-d). The cause for these fresher surface waters is not yet well understood. Most likely it is linked to reduced sea ice formation that we discuss in the next section.

175 3.3 Sea ice

The extent and thickness of sea ice in March in the Arctic Ocean and the Nordic Seas is shown in Fig. 4. We compare the sea ice thickness to average thickness (1979–2005) of the Pan-Arctic Ice-Ocean Modeling and Assimilation System (PIOMAS) reanalysis (Zhang and Rothrock, 2003; Schweiger et al., 2011). We define the ice edge as the 15 % ice concentration and compare it with the EUMETSAT OSI SAF (OSI-409-a; v1.2) product (1979–2005) (EUMETSAT Ocean and Sea Ice Satellite
180 Application, 2015).

The ice extent is largest in the reference simulation with the PP scheme (Fig. 4a). The ice edge extends further south everywhere than in PIOMAS, especially in the Nordic Seas and the Labrador Sea. The ice edge in the Labrador Sea and the Nordic Seas lies further north in all simulations with KPP and TKE, especially in HR_{ide} . In the North Pacific, the ice edge is

less affected and lies only further north in the Sea of Okhotsk in HR_{ide} . The more northerly location of the ice edge in the KPP
185 and TKE simulations results from warmer water temperatures in the Nordic Seas and Labrador Sea, which causes the sea ice
to retreat.

Ice thickness is lower in all simulations than in PIOMAS, especially in the central Arctic and north of Greenland, and lowest
in HR_{ide} . What causes thinner ice in the simulations with KPP and TKE is unclear and remains for further investigation. It
could be related to lower ice production in the marginal seas, especially in the Laptev Sea, and could require further tuning of
190 the lead-close parameterisation.

In the southern hemisphere there is also thinner ice simulated with the TKE and TKE+IDEMIX scheme for the time-averaged
September (Fig. 5), especially along the coast of Antarctica. However, we note a closed sea ice cover in the Weddell Sea in
 HR_{ide} that reduces spurious convection within the Weddell Sea polynya (see more details in section 4.4.1). The sea ice extent
is larger than in OSI SAF, but differs only slightly between the simulations.

195 3.4 Ocean interior

3.4.1 Horizontal maps of hydrographic biases

At intermediate depth, all simulations are too warm compared to EN4, as shown by the temperature bias for the model layer
at 740 m depth (Fig. 6). Exceptions are the Southern Ocean and parts of the North Atlantic, where the ocean is colder at upper
to intermediate depth. In the Atlantic Ocean, the warm biases are mainly linked to the representation of the Agulhas Current
200 system and Mediterranean Overflow water (MOW), as well as to the pathway of the Gulf Stream. Previous studies with MPI-
ESM1.2 have shown that these warm biases diminish with increasing spatial resolution (Gutjahr et al., 2019; Putrasahan et al.,
2019). Advection of these warmer (and more saline) water masses causes subsequent warm biases in the SPNA, Nordic Seas
and Arctic Ocean. Even though an eddy-resolving resolution (0.1°) reduces most of these biases, as shown by Gutjahr et al.
(2019) with MPI-ESM1.2-ER, the choice of the vertical mixing scheme also affects the hydrographic biases, for instance the
205 warm bias is reduced in the Arctic Ocean but enhanced for the MOW (Fig. 6).

Salinity shows a similar bias pattern at intermediate depth (Fig. 8). The Atlantic is too saline, which is again due to the poor
representation of the MOW and the Agulhas Current system. Consequently, northward advection by the Gulf Stream and the
boundary currents along the European shelf distribute these saline waters into the SPNA and Nordic Seas, where they affect
to local water masses (Reid, 1979; McCartney and Mauritzen, 2001; Lozier and Sindlinger, 2008). At a resolution of 0.4° ,
210 MPI-ESM1.2-HR is unable to capture the Agulhas Retroflexion. Although all simulations show a similar salinity bias in the
Agulhas region, we note a larger bias for HR_{kpp} , HR_{tke} , and HR_{ide} . This larger bias indicates a stronger inflow of warm and
salty water from the Indian Ocean. In fact, the inflow is about 10 Sv stronger with TKE and about 15 Sv with KPP than the 40
to 50 Sv in HR_{pp} (Fig. 7).

The largest difference in salinity bias is linked to the representation of MOW. Although all models produce warmer and more
215 saline MOW, the bias is decreased only in HR_{tke} . The bias even becomes considerably larger when TKE is used with IDEMIX
instead of an artificial background diffusivity (Fig. 8d). Although the use of IDEMIX increases vertical eddy diffusivity at

the overflow sill of the Strait of Gibraltar and in the Gulf of Cádiz (not shown), downstream vertical mixing over the abyssal plains of the Atlantic is very low, probably due to the low internal wave activity, so that the diffusivity becomes very low ($O(10^{-6} \text{ m}^2 \text{ s}^{-2})$). We speculate that this lower diffusivity reduces mixing with the overlying, less saline North Atlantic Central Water, so that the warm, highly saline core of the MOW is less diluted than in the other simulations. However, it remains a subject of further investigation whether warmer and especially saltier MOW with IDEMIX is related to other influencing factors, such as the variability of the near-surface wind field or the net evaporation over the Mediterranean Sea (Aldama-Campino and Döös, 2020).

We further note a slight freshwater bias in the Arctic Ocean in HR_{ide} that we will describe in relation to the Atlantic water layer in section 4.2.

3.4.2 Vertical sections through the Atlantic and Arctic Ocean

A vertical section of the zonally averaged potential temperature bias through the Atlantic and Arctic Oceans (Fig. 9) shows predominantly too cold near-surface water, especially in the North Atlantic, where the cold bias extends to a depth of about 1000 m due to errors in heat convergence resulting from a misrepresented Gulf Stream and North Atlantic Current. The intermediate water masses are too warm compared with EN4 and there appears almost no bias in the deeper ocean, since the simulation length is too short to affect the abyssal ocean. This general bias pattern establishes in all simulations, but we note some differences.

All simulations simulate a too warm (and saline) inflow of from the Indian Ocean to the South Atlantic, roughly at 30°S . The model resolution is too coarse to correctly capture the Agulhas Current system; in particular, the retroflexion and Agulhas rings are not well represented. Instead, warm and saline water flows more or less constantly from the Indian Ocean into the South Atlantic. From all simulations, this misrepresentation is strongest in HR_{ide} . The reason for this behaviour remains a subject for future studies.

A second source of too warm water is related to the MOW, as described above. The core of the MOW reaches a neutral buoyancy surface slightly above 1000 m depth at roughly 30°N . The MOW is warmest in HR_{ide} but colder in HR_{tke} compared to the reference simulation.

These already too warm waters are transported north throughout the whole Atlantic and eventually reach the SPNA and Nordic Seas. Part of it continues further into the Arctic Ocean at a depth of 500 m to more than 1000 m, where it becomes the Atlantic water (AW) layer, which is roughly 1°C warmer than in EN4. Due to stronger recirculation in Fram Strait (see section 4.2), less AW enters the Arctic Ocean in HR_{ide} , reducing the warm bias.

The Nordic Seas, but also the Labrador Sea, is thus already too warm when overflow water is generated, leading to too warm overflows across the Greenland-Scotland Ridge at and south of 60°N , reaching depths of about 3000 m. Warmer temperatures in the Nordic Seas compensate at least partly for the increased salinity, so that the increase in density is less. Since the Nordic Seas are warmest in HR_{kpp} , the overflows are also warmest in this simulation.

Salinity shows a similar bias pattern (not shown) with too saline waters where there is a warm bias.

250 3.5 AMOC and transports

The SPNA and the Nordic Seas are important regions for the global climate, where the vertical connection between the upper warm and the lower cold branch of the AMOC is established. The northward flowing warm AW is cooled by extensive heat loss to the atmosphere until it becomes dense enough to sink into deeper layers. Together with the dense overflow water from the Nordic Seas, it leaves the SPNA as North Atlantic Deep Water (NADW) with the southward-flowing Deep Western Boundary
255 Current (DWBC).

The simulations with KPP and TKE produce a stronger and deeper reaching upper branch of the AMOC of $> 18\text{ Sv}$ at 26.5°N (Fig. 10) compared with about 15 Sv in HR_{pp} . A stronger upper cell may imply a stronger northward heat transport, whereas a deeper upper cell indicates a stronger southward transport of NADW (see section 4.1.2). To compare the enhanced overturning in the Nordic Seas, the water in the Atlantic has to be replaced by stronger inflow from the Indian Ocean that
260 establishes in the simulations with KPP and TKE.

We note, however, that the bottom cell is weaker in all sensitivity simulations, which is probably due to a stronger mixing of NADW with Antarctic Bottom Water (AABW), causing the latter to vanish further south. The simulation length of 100 years is too short to see pronounced effects in the deep ocean, but it could be expected that over longer periods (several centuries) the additional mixing from internal waves might affect the diapycnal diffusion of the upwelling deep water, e.g. in the Pacific.

265 4 Effects on the regional ocean

In this section, we discuss some regional areas in more detail, in particular the Atlantic Ocean, the Nordic Seas and Fram Strait, the Arctic Ocean, and the Southern Ocean. We already note here that the insufficient model resolution determines the large-scale bias pattern, as shown by Gutjahr et al. (2019).

4.1 Subpolar North Atlantic and the Nordic Seas

270 4.1.1 Convection and mixed layer depths

The sinking of buoyant Atlantic water is thought to be established by downwelling of dense water along the boundary currents with complex interplay of deep convection and the mesoscale eddy field (e.g. Katsman et al., 2018; Brüggemann and Katsman, 2019; Sayol et al., 2019; Georgiou et al., 2019). The water mass transformation of Atlantic water occurs, however, in areas of deep convection and lateral exchange with the boundary current by eddies. Convection, or vertical instability, is parameterised
275 differently in the vertical mixing schemes in MPI-ESM1.2 (see Appendix A), which is why we expect differences in vertical diffusion and mixed layer depths (MLDs). Eddies are only partially resolved in MPI-ESM1.2-HR, so we do not expect the exchange of deep water with the boundary currents to be realistic.

The largest diffusivities (K) are simulated in the Labrador Sea and the Nordic Seas (Fig. 11), with markedly greater values in the simulations with KPP and TKE. In particular, we note increased vertical diffusivities in the Irminger Sea, where open-ocean
280 deep convection occurs and contributes to the formation of Labrador Sea water (e.g. Pickart et al., 2003; Våge et al., 2011).

In the PP scheme, the vertical instability is parameterised by enhancing the diffusivity to $K = 0.1 \text{ m}^2 \text{ s}^{-1}$. The convection parameterisation in KPP is more complex, where non-local transport terms (see section A2) redistribute the surface fluxes throughout the ocean surface boundary layer. These non-local transport terms depend on the net heat and freshwater fluxes at the ocean surface, on K , and on a dimensionless vertical shape function (Large et al., 1994; Griffies et al., 2015).

285 In the TKE scheme, the buoyancy term (third term on the r.h.s. of Eq. A15), which usually is an energy transfer from TKE to mean potential energy, acts in this case ($N^2 < 0$) in the opposite direction and enhances TKE. However, besides differences in the parameterisations, remotely changed water mass properties, and hence density changes, also affect convection and the MLD in the SPNA. Therefore, it is not straightforward to diagnose what is a cause and what is a consequence for changes in the MLDs.

290 The average MLDs in March are shown in Fig. 12. A direct comparison with MLDs derived from Argo floats are not optimal, because our simulations are control simulations with 1950s greenhouse gas forcing. Keeping this in mind, we find profound differences to Argo float-derived MLDs and across the simulations. As with vertical diffusivity, all simulations show the deepest mixed layers in the Labrador Sea and a second maximum in the GIN Seas. In general, KPP and TKE tend to simulate deeper mixed layers. In the Labrador Sea, the convection area extends too far north in all simulations due to the
295 lack of mesoscale eddies that would impede convection by restratification of the water column (e.g. Eden and Böning, 2002; Brüggemann and Katsman, 2019; Gutjahr et al., 2019). HR_{ide} simulates deeper mixed layers in the centre of the Greenland Sea gyre and particular around Jan Mayen, which might be caused by internal wave activity, especially along the Kolbeinsey and Mohn Ridge and along the Jan Mayen Fracture Zone.

Due to stronger updoming of the isopycnals in the Labrador, Irminger and Greenland Sea in the simulations with KPP and
300 TKE, the strength of the gyres are stronger than in HR_{pp} (Fig. 13). This enhanced updoming is caused by a combination of a more saline SPNA and Nordic Seas, e.g. about $+0.2$ psu in the Greenland Sea, and enhanced heat loss in the gyre centres. The steeper isopycnal gradients accelerate the geostrophic flow around the convection centres leading to a roughly 10 Sv stronger boundary current in the Labrador Sea and a Greenland gyre that is about 5 Sv stronger.

4.1.2 Overflows from the Nordic Seas

305 A substantial contribution to the NADW constitutes the Denmark Strait overflow water (DSOW; $\sigma > 1027.8 \text{ kg m}^{-3}$), which accounts for about half of the observed overflows from the Nordic Seas (Hansen et al., 2004), being its densest water mass. The other major overflow pathway across the Greenland-Iceland-Scotland Ridge is through the Faroe Shetland Channel (FSC; $\sigma > 1027.75 \text{ kg m}^{-3}$) and through the Faroe Bank Channel (FBC; $\sigma > 1027.75 \text{ kg m}^{-3}$).

The increased MLDs in the simulations with KPP and TKE due to stronger deep convection in the Nordic Seas suggest
310 higher overflow volumes. We applied Welch's two-sided t-tests with $\alpha = 0.05$ ($n = 20$) to test for significant differences in the simulated overflows. See Tab. A1 for all test results.

First we note that all simulations underestimate the observed DSOW volume transport of about 3.2 to 3.4 Sv by roughly 1 Sv (see Tab. 2). Compared with HR_{pp} , however, we find about 10 to 20 % higher DSOW transports in HR_{kpp} , HR_{ide} and especially in HR_{tke} (all with $p < 0.01$). The transports in the KPP and TKE simulations themselves, however, differ not significantly (p -

315 values of 0.13 to 0.52). The higher amount of DSOW might thus explain at least partly the stronger upper cell of the AMOC, and in particular the AMOC strength around 60°N.

Although overestimated compared to the observations, the FSC overflows in the simulations are of similar magnitude (3.2 to 3.3 Sv), with the exception of HR_{tke}, which produces an approximately 10 % higher (3.5 Sv) overflow transport ($p < 0.01$). The FBC overflows are about 15 to 20 % lower in the models (1.7 to 1.9 Sv) than the observed 2.2 Sv by Hansen et al. (2016).
320 The deviations between the models are of the order of 10 %, with a higher mean transport in HR_{tke} ($p < 0.01$) and a lower transport in HR_{ide} ($p < 0.01$).

Overall, these results suggest about 10 % higher overflow transports across the Greenland-Iceland-Scotland ridge with KPP and TKE, which contribute to a stronger upper cell of the AMOC.

4.2 Fram Strait and Atlantic water layer

325 Atlantic water (AW) is the main supplier of salt and oceanic heat to the Arctic Ocean. From the Nordic Seas it flows northwards into Fram Strait, where about half of the AW recirculates southwards between 76° and 81°N and becomes part of the East Greenland Current. A smaller fraction continues northward as the West Spitsbergen Current (WSC). Due to the successive cooling in its path, the subsiding AW water flows into the Arctic Ocean at mid-depth with its core at about 400 m depth, sealed off from the atmosphere by overlying cold polar surface water.

330 A common error of many state-of-the-art ocean models is an anomalously thick and deep AW layer (e.g. Holloway et al., 2007; Shu et al., 2019). This error is thought to be related to model resolution and to vertical mixing parameterisations, in particular to the choice of the background diffusivity (Zhang and Steele, 2007; Liang and Losch, 2018). In terms of model resolution, it was recently shown that a high-resolution ocean (0.1° or better) reduces biases of the AW layer (Wang et al., 2018; Gutjahr et al., 2019), because eddies are (partly) resolved that also improve the circulation (Wekerle et al., 2017). MPI-
335 ESM-HR at eddy-permitting resolution produces a too warm AW layer, as shown by Gutjahr et al. (2019). Here, we demonstrate that this warm bias is reduced by using TKE+IDEMIX, which is due to a combination of remote (already colder inflowing AW into Fram Strait) and local effects (stronger southward recirculation at Fram Strait and stronger heat loss due to enhanced mixing).

In HR_{pp}, HR_{kpp}, and HR_{tke} the warm bias of the AW layer is about +2°C at the Yermak Plateau (YP), a bathymetric feature
340 northwest of the Svalbard archipelago known as a hotspot for internal wave activity (see also Fig A2b) and mixing (e.g. Fer et al., 2010; Crews et al., 2019), and less further downstream along the shelf break of the Eurasian Basin (Fig. 14). It seems that a part of the AW also crosses the Lomonosov Ridge, except in HR_{ide}, and spreads into the Markarov and Canada basins, which is not realistic. The AW is colder in HR_{ide} and better agrees with EN4 in the Eurasian basin, although the central Arctic Ocean becomes about 0.5°C too cold.

345 Due to stronger heat loss in the Greenland Sea (not shown) the Atlantic water is already about 1°C colder in HR_{ide} compared with the other simulations when it reaches Fram Strait, although warmer AW could be expected due to the stronger Greenland Sea gyre (Chatterjee et al., 2018; Muilwijk et al., 2019). This contradiction can be explained by a stronger recirculation of AW in HR_{ide} in Fram Strait, which means that less AW flows in the Arctic Ocean and thus less heat.

Beside this remote effect, there are local effects related to enhanced mixing at the YP. A comparison of K of the model layer
350 at 450 m depth (Fig. 15) shows that the mixing near YP in HR_{ide} is slightly stronger (Fig. 15d). Internal waves break near the
YP and thus transfer energy to small-scale turbulence. This effect is larger in the prognostic IDEMIX than from the assumed
constant background diffusivity. The increased mixing in the ocean causes more heat loss, as more warm AW is exposed to
the cold atmosphere, and thus cools more efficiently than in the other simulations. In fact, the sensible heat flux is about 20
to 40 W m^{-2} larger in HR_{ide} than in HR_{pp} (not shown). For comparison, the sensible heat flux is only about 10 to 20 W m^{-2}
355 stronger in HR_{kpp} and HR_{tke} .

4.3 Arctic Ocean

Although largely unknown, sparse observations indicate that turbulence in the Arctic Ocean is typically weak (Rainville and
Winsor, 2008; Fer, 2009). The wind stress cannot act on the sea surface because of the insulating sea ice cover, which is why
the effect of the wind stress on vertical mixing decreases quadratically with the sea ice concentration in the simulations with
360 PP and KPP (see Appendix A). In addition, brine rejection is less effective as a mixing mechanism because of the strong
vertical salinity gradients in the cold halocline layer. Therefore, apart from enhanced mixing by episodic shear events, storms
during ice-free conditions (Rainville and Woodgate, 2009), mesoscale eddies, or lateral intrusion along the boundaries, vertical
diffusive mixing dominates over turbulent mixing (Fer, 2009).

Internal wave activity is almost absent, except above rough topographic features. In fact, internal waves are trapped at the
365 place of their origin and do not propagate far into the Arctic Ocean. This trapping occurs because the Arctic Ocean is north of
the critical latitude, which is 74.5°N for the M_2 tide, beyond which the Earth's rotation prohibits freely propagating internal
waves. As a result, they dissipate at or very close to their source region with properties similar to lee waves (Rippeth et al.,
2015, 2017).

For this reason, there is little or no contribution to small-scale turbulence in the inner Arctic Ocean in HR_{ide} , especially in the
370 deep and flat-bottomed Canada basin. The eddy diffusivity K is up to two orders of magnitude smaller ($O(10^{-6}$ to $10^{-7} \text{ m}^2 \text{ s}^{-1})$)
in HR_{ide} compared to the other simulations (Fig. 15), in which K is mostly at the constant background value ($1.05 \cdot 10^{-5} \text{ m}^2 \text{ s}^{-1}$).

Representing this trapping of internal waves is crucial to simulate eddy diffusivities that are more consistent with mi-
crostructure measurements, which show low eddy diffusivities in deep, flat-bottomed basins, but elevated diffusivities above
deep topography (Rainville and Winsor, 2008). The low diffusivities in deep basins agree well with observations from the
375 Barneo ice camp drift, where $O(10^{-6} \text{ m}^2 \text{ s}^{-1})$ was measured below the mixed layer in the Amundsen Basin (Fer, 2009).

Lower vertical diffusivity under sea ice in the Arctic Ocean might cause denser water to enter the Nordic Seas (Kim et al.,
2015), which could then lead to denser overflows across the Greenland-Iceland-Scotland Ridge and a 14 % stronger upper cell
of the AMOC. Indeed, HR_{ide} generates higher overflow volumes and a 10 % stronger AMOC, but these are probably caused
more by denser water masses in the Greenland Sea. However, we cannot rule out the effect of denser water from the Arctic
380 Ocean.

A contrasting example of higher diffusivities in the inner Arctic Ocean is a distinct band of strong mixing along and above the Lomonosov Ridge (Fig. 15d). Here, internal waves break immediately after their formation and thus locally increase the small-scale turbulence, a process that was also directly measured by Rainville and Winsor (2008).

Assuming a constant background diffusivity thus largely overestimates the vertical mixing in the Arctic Ocean. Although
385 the background diffusivity can be artificially reduced to mimic this low internal wave activity (e.g. Kim et al., 2015; Sein et al., 2018), the very heterogeneous pattern described above would not be captured. The combination of TKE with IDEMIX is able to reproduce the spatial pattern and the correct magnitudes. It further provides an energetically more consistent solution that should be preferred.

4.4 Southern Ocean and Weddell Sea

390 4.4.1 Open-ocean convection in the Weddell Sea polynya

A well-known problem in ocean modelling is a too frequent semi-permanent Weddell Sea polynya caused by false deep convection bringing warm Circumpolar Deep Water (CDW) close to the surface (Sallée et al., 2013; Kjellsson et al., 2015; Heuzé et al., 2015; Stössel et al., 2015; Naughten et al., 2018). Possible explanations are insufficient freshwater supply (Kjellsson et al., 2015), mainly due to a lack of glacier melt water (Stössel et al., 2015), and insufficient wind mixing in summer (Timmermann and Beckmann, 2004; Sallée et al., 2013; Kjellsson et al., 2015), which causes a high salinity bias in the mixed layer that
395 erodes the stratification; see a more detailed discussion in Gutjahr et al. (2019). In contrast to this view, Dufour et al. (2017) argue that deep convection in the Weddell Sea does not necessarily lead to an open-ocean polynya, because strong vertical mixing in low-resolution models inhibits the built-up of a subsurface heat reservoir that would be necessary for intermittent Weddell Sea polynyas.

400 We do not expect a realistic representation of the Weddell Sea polynya in our MPI-ESM1.2-HR 1950s control simulations, because they should develop intermittently only under pre-industrial conditions and grow out from Maud Rise polynyas (de Lavergne et al., 2014; Gordon, 2014; Kurtakoti et al., 2018; Campbell et al., 2019; Cheon and Gordon, 2019; Jena et al., 2019), for which high resolution (0.1° or better) is required (Stössel et al., 2015; Dufour et al., 2017).

Although all simulations produce these semi-permanent Weddell Sea polynyas and thus too deep mixed layers (Fig. 16), the
405 area of excessive deep convection is reduced in HR_{ide} (Fig. 16e). Similarly, too deep mixed layers are simulated in the Ross Sea, except in HR_{tke} , which simulates shallower mixed layers without further reduction when using IDEMIX (HR_{ide}). The Weddell Gyre is also linked to the Antarctic Circumpolar Current (ACC; Orsi et al., 1993; Cheon et al., 2019), because it controls the inflow of relatively warm and saline CDW into the inner Weddell Sea, possibly eroding the weak stratification and triggering deep convection. The simulated ACC transports through Drake passage (Tab. 3) are close to the recently observed $173.31 \pm$
410 $10.7 Sv$ (Donohue et al., 2016), whereby HR_{tke} achieves the best estimate with $174 Sv$. Simulations with lower convection in the Weddell Sea produce lower transports of about 161 to 163 Sv (HR_{pp} and HR_{ide}), whereas HR_{kpp} produces a much higher transport of 192 Sv because of steeper isopycnals due to enhanced convection in the Weddell Sea. Since eddies are not resolved and the GM coefficient is rather low, there is no or too little eddy compensation to flatten the isopycnals.

One possible explanation why HR_{ide} simulates less convection in the Weddell Sea is that IDEMIX creates more mixing
415 above the shelf, which spreads near-surface freshwater laterally into the centre of the Weddell Gyre much more efficiently (not
shown). Fresher conditions in the Weddell Gyre favours the formation of sea ice, which insulates the ocean from further heat
loss and thus impedes convection. In HR_{ide} , the average sea ice concentration in September is about 50 to 70 % in the Weddell
Gyre (not shown), whereas it is considerably lower in the other simulations with concentrations of 20 to 50 %. Furthermore,
the ice is also thicker with IDEMIX compared with the other simulations (Fig. 5d). Although the sea ice concentration is still
420 too low, the spurious deep convection in the Weddell Sea is reduced with IDEMIX.

4.4.2 Deep Mixing Band in the Southern Ocean

Another challenge for current ocean models is the representation of the Deep Mixing Band (DMB; DuVivier et al., 2018),
which extends from the western Indian Ocean to the eastern Pacific Ocean and reaches MLDs of more than 700m (Holte et al.,
2017, Fig. 16a). The DMB builds up over the winter months and is deepest in September. Subantarctic Mode Water (SAMW;
425 McCartney, 1977) forms in the DMB near the Subantarctic Front, just north of the ACC. The SAMW acts as an important
carbon sink (e.g. Sabine et al., 2004) and it ventilates the mid-deep ocean (e.g. Sloyan and Rintoul, 2001; Jones et al., 2016),
replenishing oxygen and nutrients (e.g. Sarmiento et al., 2004). It was shown that high resolution (0.1°) leads to deeper and
thus more realistic MLDs in the DMB (Li and Lee, 2017; DuVivier et al., 2018; Gutjahr et al., 2019), but it is thought that
fundamental vertical physics are missing in ocean models (DuVivier et al., 2018).

430 Although HR_{pp} reproduces the DMB in the Indian Ocean, the mixed layers are too shallow in almost the entire Pacific
sector (Fig. 16b). KPP and TKE improve the representation of the DMB in the Pacific Ocean and simulate deeper mixed
layers, especially in the Indian Ocean. The MLDs are close to observations (Fig. 16c-e), albeit with a too wide DMB, which
is probably caused by insufficient model resolution, since it becomes much narrower when an eddy-resolving model is used
(Gutjahr et al., 2019). The choice of a mixing scheme other than PP has little influence on the MLDs, except south of Tasmania,
435 where TKE appears to produce the deepest mixed layers.

Although not observed by Argo floats, but common to all simulations are deeper mixed layers north of 50°S in the Pacific
Ocean east of New Zealand and in the South Atlantic. However, it should be kept in mind that comparing model simulations
with Argo float data is always difficult, because the floats do not measure continuously in time and space and, in addition, we
compare them with control simulations.

440 5 Effects on the atmosphere

From section 3 the question arises whether atmospheric variables are influenced by a changed vertical mixing scheme. We
briefly compare key quantities of the atmosphere and use ERA-Interim (Dee et al., 2011) from the period 1979–2005 as
reference. This period and data was used to tune the atmospheric component ECHAM6.3 of the MPI-ESM1.2.

5.1 Near-surface fields

445 The 2 m air temperature (SAT; Fig. 17) is closely related to the SST and we find distinct effects on the bias by changing the vertical mixing scheme, not only over the ocean but also over land (Fig. 17). In the reference simulation (HR_{pp}) the pattern widely agrees with the SST bias (see section 3.4) with a pronounced cold bias in the North Atlantic and in the Nordic Seas. These cold biases seem to affect most parts of Europe as well. The most pronounced warm bias in the northern hemisphere extends over large parts of Canada and over the Labrador Sea. The warm bias over the Labrador Sea is related to an over-
450 extended area of convection (Fig. 12) that prevents the sea ice from extending far enough south (Fig. 4), causing the air masses over the open ocean to become too warm. In the sensitivity simulations, we find a reduction of the cold bias in the North Atlantic and in particular in the Greenland, Barents and Kara Seas. However, as with the SST bias, the air temperature over the subpolar gyre becomes warmer; in particular over the Labrador Sea, where all sensitivity simulations produce a larger convection area and less sea ice cover.

455 In the Southern Ocean, the SAT is too cold along the ACC by about 1 °C and colder to the west of the Antarctic peninsula. The air temperature above the Weddell Sea, is warmer than in ERA-Interim, especially when using TKE, because of the large sensible heat fluxes from the Weddell Sea polynya. However, even though IDEMIX reduces the area and intensity of this polynya, there is no effect on the SAT, which requires further investigation in a future study.

Other quantities, such as wind speed or precipitation are not affected by changing the vertical mixing scheme in the ocean.

460 5.2 Zonal temperature and velocity

The zonally averaged global air temperature is mostly too cold (Fig. 18) in the entire troposphere and too warm in the stratosphere compared to ERA-Interim. Warmer SSTs in the northern hemisphere with KPP and TKE propagate to higher layers of the troposphere. While warmer temperatures remain limited to the extratropics of the northern hemisphere in HR_{tke} in comparison to HR_{pp} (significant at the 5 %-level), also the tropics and the southern hemisphere become warmer with KPP, which
465 produces also the warmest troposphere.

The warmer extratropics with TKE result in a weaker meridional gradient that reduces the thermal wind and leads to a weaker jet stream in the northern hemisphere (Fig. 19c-d). However, in HR_{kpp} (Fig. 19b), no weakening of the northern hemispheric jet stream is seen, most likely because meridional gradients are maintained when the entire hemisphere is uniformly warmer.

6 Conclusions

470 We have compared the effect of four different ocean vertical mixing schemes (PP, KPP, TKE, TKE+IDEMIX) on the ocean mean state in MPI-ESM1.2-HR simulations. The ocean mixing library CVMix (Griffies et al., 2015), which we extended with the TKE and TKE+IDEMIX schemes, allowed for a side-by-side comparison of these schemes.

From the results described above emerges a consistent picture. Using KPP or TKE increases the convection in the SPNA and Nordic Seas, but also in the southern hemisphere. Due to enhanced convection, the overflows from the Nordic Seas

475 increase by about 10 %. Stronger overflows and increased inflow from the Indian Ocean into the South Atlantic result in a
stronger and deeper upper cell of the AMOC. The roughly 3 Sv (or 20 %) stronger AMOC transports more heat and salt into
the SPNA and its marginal seas. The higher salinity favours deep convection, maintaining a stronger AMOC, whereas the
higher heat transport increases the SSTs. The warmer SSTs affect the atmosphere, resulting in warmer extratropics with TKE,
weakening the meridional temperature gradient and thus the jet stream in the northern hemisphere. With KPP, the tropics and
480 the southern hemisphere also become warmer, but without weakening of the jet stream due to a more uniform warming. These
results highlight the clear advantage of using coupled models in which the surface state can evolve interactively, rather than air
temperature or salinity being dictated by restoring as in ocean-only configurations.

KPP, TKE and TKE+IDEMIX produce similar results, but differ in some aspects. Most pronounced is that IDEMIX pro-
duces a more heterogeneous spatial pattern of vertical diffusivity, with generally lower values in deep and flat basins and
485 increased turbulence over rough topography. This spatial pattern is particularly evident in the Arctic Ocean and fits better with
microstructure measurements without having to artificially lower the background diffusivity.

In addition, IDEMIX improves the circulation and mixing in the Nordic Seas and in the Fram Strait, which reduces the warm
bias of the Atlantic water layer in the Arctic Ocean. In the Southern hemisphere, IDEMIX reduces the spurious deep convection
in the Weddell Sea because of enhanced mixing above the shelf that seems to increase the lateral transport of freshwater into
490 the inner Weddell Sea, thereby impeding deep convection. The main advantages of IDEMIX is its energetically more consistent
formulation without assuming an artificial background diffusivity and its flexibility that allows additional energy inputs, e.g.
from the mesoscale eddy field.

Code and data availability. Model codes developed at MPI-M are intellectual property of MPI-M. Permission to access the MPI-ESM source
code can be requested after registering at the MPI user forum (<https://www.mpimet.mpg.de/en/science/models/mpl-esh/users-forum/>, last
495 accessed August 2020) and may be granted after accepting the MPI-M Software License Agreement ([https://www.mpimet.mpg.de/fileadmin/
models/MPIESM/mpl-m_sla_201202.pdf](https://www.mpimet.mpg.de/fileadmin/models/MPIESM/mpl-m_sla_201202.pdf)).

After registration, the model source code is accessible from https://doi.org/10.35089/WDC/PRIMAVERA_MPI_ESM_source_code us-
ing branch *mpiesm-1.2.01-cvmix_GMD* for the KPP, TKE, and TKE+IDEMIX simulations and *mpiesm-1.2.01-primavera_PP_GMD* for the
PP simulation. Primary data and scripts used in the analysis, and other supplementary information that may be useful in reproducing the
500 author's work can be obtained from MPI PuRe (<http://hdl.handle.net/21.11116/0000-0006-DB1E-3>). Initial fields and all forcing fields can
be downloaded from DKRZ LTA DOCU (https://cera-www.dkrz.de/WDC/ui/cersearch/entry?acronym=DKRZ_LTA_944_ds00001). The
model code used for the simulations in the paper and the primary data have been provided to the anonymous reviewer and the topical editor.

Appendix A: Ocean vertical mixing schemes in MPI-ESM1.2

In this section we give a brief summary of the ocean vertical schemes that we have implemented into MPI-ESM1.2. The vertical
505 mixing schemes were implemented via the Community Vertical Mixing (CVMix) library (Griffies et al., 2015; Van Roekel

et al., 2018), except for the PP scheme. The KPP schema was already part of the CVMix library, which we therefore extended with the TKE and IDEMIX scheme. This extension will become part of the official CVMix library.

The schemes below aim to parameterise the vertical turbulent fluxes following this general flux-gradient or K-profile approach:

$$510 \quad \overline{w'\lambda'} = -K_\lambda \left(\frac{\partial \Lambda}{\partial z} \right) + \Gamma_\lambda, \quad (\text{A1})$$

with w' the vertical turbulent velocity, λ' the turbulent fluctuation of a quantity, λ a grid-scale quantity and the turbulent exchange coefficient ($K_\lambda > 0$) or also termed eddy viscosity for momentum flux and eddy diffusivity for tracer fluxes, such as temperature or salinity. Γ_λ represents any flux not proportional to the local gradient $\partial_z \Lambda$ and is referred to as *nonlocal flux*. In our comparison, Γ_λ is only accounted for in the KPP scheme (A2).

515 **A1 Pacanowski and Philander (1981, PP) scheme**

In our control simulation the vertical turbulent diffusion and viscosity are based on a modified version of the Richardson-number dependent formulation by Pacanowski and Philander (1981) (PP scheme). The modifications are that (1) the vertical diffusivity is not dependent on the vertical viscosity, and (2) that the turbulent mixing in the ocean mixed layer is assumed to depend on the cube of the 10 m wind speed (Marsland et al., 2003). This dependency decays exponentially with depth and with
520 potential density difference to the surface. Since the classical approach by Pacanowski and Philander (1981) underestimates the turbulent mixing close to the surface (Marsland et al., 2003), this additional wind induced mixing (κ_w) is added, and defined as:

$$K_w(1) = (1 - A)^2 w_t U_{10}^3 \quad (\text{A2})$$

$$K_w(k) = K_w(k-1) \frac{\frac{\lambda}{\Delta z}}{\frac{\lambda}{\Delta z} + \delta_z \rho} e^{-\frac{\lambda}{z_0}} \quad (\text{A3})$$

525 with $k = 2, 3, \dots, n$ the vertical model level, Δz the layer thickness, A the fractional sea ice concentration, U_{10} the 10 m wind speed, $w_t = 0.5 \cdot 10^{-3} / 6.0^3$, $\lambda = 0.03$, and $z_0 = 40.0$ (e-folding depth) are adjustable parameters, and $\delta_z \rho$ the local static stability.

The total equation for the eddy vertical diffusivity then reads:

$$K_d(z) = \frac{d_{v,0}}{(1 + c_d Ri(z)^2)} + K_w(z) + d_{v,b}, \quad (\text{A4})$$

530 with $d_{v,0} = 0.2 \cdot 10^{-2} \text{ m}^2 \text{ s}^{-1}$, $c_d = 5.0$, and the background diffusivity $d_{v,b} = 5 \cdot 10^{-5} \text{ m}^2 \text{ s}^{-1}$. The eddy vertical viscosity is parameterised as:

$$K_v(z) = \frac{a_{v,0}}{(1 + c_d Ri(z)^3)} + K_w(z) + a_{v,b}, \quad (\text{A5})$$

with $a_{v,0} = 0.2 \cdot 10^{-2} \text{ m}^2 \text{ s}^{-1}$, $c_a = 5.0$, and $a_{v,b} = 1.05 \cdot 10^{-5} \text{ m}^2 \text{ s}^{-1}$ the background viscosity. The eddy coefficients K_d and K_v are partially relaxed to the value at the previous time step by use of a time filter to avoid $2\Delta t$ oscillations (Marsland et al., 2003). Convection is parameterised as enhanced diffusivity ($K_d = 0.1 \text{ m}^2 \text{ s}^{-1}$) for the PP scheme.

A2 K-profile parameterisation (KPP) scheme

The second simulation uses the K-profile parameterisation (KPP scheme) from Large et al. (1994) for the mixed layer. In general, a turbulent flux ($\overline{w'\lambda'} = \overline{w\lambda}$) of a quantity Λ (momentum, scalar tracers) are parameterised as:

$$\overline{w\lambda} = -K_\lambda \left(\frac{\partial \Lambda}{\partial z} \right) + K_\lambda^{\text{non-local}} \gamma_\lambda, \quad (\text{A6})$$

with K_λ the local diffusivity for tracers or viscosity for momentum, z the depth, $K_\lambda^{\text{non-local}}$ the non-local diffusivity/viscosity, and a non-local term γ_λ . While the local flux (first term on the right hand side) depends directly on the local gradient of a quantity, the non-local flux (second term on the right hand side) redistributes the surface fluxes throughout the whole surface boundary layer, for example due to convection (see below).

The local diffusivity (K_λ) is calculated as:

$$K_\lambda(\sigma) = h w_\lambda(\sigma) G(\sigma), \quad (\text{A7})$$

with $\sigma = z/h$ the dimensionless vertical coordinate ($0 \leq \sigma \leq 1$), z the depth below the sea surface, h the ocean boundary layer depth, w_λ a vertical turbulent velocity scale (either for scalar tracers or momentum), and $G(\sigma) = \sigma(1 - \sigma)^2$ a universal shape function. Oftentimes, and also in our implementation, it is assumed that $K_\lambda^{\text{non-local}} = K_\lambda$ (Griffies et al., 2015).

The ocean boundary layer depth h is determined at the depth z where the bulk Richardson-number Ri_b becomes larger than a critical Richardson-number $Ri_c = 0.3$. The bulk Richardson-number at depth z is defined as:

$$Ri_b(z) = \frac{(z - z_{sl}) [B_{sl} - B(z)]}{|\mathbf{U}_{sl} - \mathbf{U}(z)|^2 + U_t(z)^2}, \quad (\text{A8})$$

with z_{sl} the depth at the centre of the surface layer (defined as $0 \leq z \leq \epsilon h$), where we assume that the surface layer is 10% ($\epsilon = 0.1$) of the ocean boundary layer depth h , as in Large et al. (1994). Since the calculation of the ocean boundary layer depth h requires Ri_b , which itself requires h , we face a cyclic problem. To solve this problem, we follow the column sampling method recommended by Griffies et al. (2015) (see details in their description).

B_{sl} is the surface layer averaged buoyancy flux, $B(z)$ the local buoyancy flux, U_{sl} the surface layer averaged velocity, $U(z)$ the local velocity and $U_t(z)$ a parameterisation for unresolved turbulent vertical velocity shear that reduces the bulk Richardson number (see e.g. Griffies et al. (2015) for the definition of the unresolved turbulent shear).

The vertical turbulent velocity scale w_λ is calculated as follows:

$$w_\lambda(\sigma) = \frac{\kappa u_* (1 - A)^2}{\Phi_\Lambda(\zeta)}, \quad (\text{A9})$$

with $\kappa = 0.4$ the von-Kármán constant, u_* the surface friction velocity that reduces with increasing fractional sea ice (A), Φ_Λ a dimensionless similarity function (momentum or scalar tracer), depending on $\zeta = \sigma h/L$, with $L = \frac{u_*^3}{\kappa B_f}$ the Monin-Obukhov length scale. B_f is the buoyancy forcing in the ocean boundary layer. Under neutral forcing ($\zeta = 0 \rightarrow \Phi_\Lambda(0) = 1$), Eq. A9 reduces to $w_\lambda(\sigma) = \kappa u_* (1 - A)^2$. We use the similarity functions of Large et al. (1994) (cf see Appendix B) for stable ($\zeta > 0$),
565 unstable ($\zeta_m < \zeta < 0$ or $\zeta_s < \zeta < 0$), and very unstable conditions ($\zeta < 0$):

$$\Phi_m(\zeta) = \begin{cases} 1 + 5\zeta & \zeta > 0 \\ (1 - 16\zeta)^{-1/4} & \zeta_m < \zeta < 0 \\ (a_m - c_m\zeta)^{-1/3} & \zeta < -\zeta_m \end{cases} \quad (\text{A10})$$

$$\Phi_s(\zeta) = \begin{cases} 1 + 5\zeta & \zeta > 0 \\ (1 - 16\zeta)^{-1/4} & \zeta_s < \zeta < 0 \\ (a_s - c_s\zeta)^{-1/3} & \zeta < \zeta_s \end{cases} \quad (\text{A11})$$

with $\zeta_m = -0.2$, $\zeta_s = -1.0$, $a_m = 1.26$, $c_m = 8.38$, $a_s = -28.86$, and $c_s = 98.96$. We do not match the diffusivities at the base of the mixed layer to avoid overshooting tracers, as recommended by Griffies et al. (2015).

570 For the non-local flux term in Eq. A6, it is assumed that $K_\lambda = K_\lambda^{\text{non-local}}$, so that this term simplifies to: $K_\lambda \gamma_\lambda$. The non-local flux γ_λ is only non-zero if $B_f < 0$ (buoyancy gain at the surface) and only for scalar tracers such as temperature, θ , or salinity, s ; for momentum it is set to zero. With the assumption $K_\lambda = K_\theta = K_s$ and a universal shape function ($G(\sigma)$), the non-local fluxes take the form:

$$\overline{w\theta}^{\text{non-local}} = K_\lambda \gamma_\theta = -G(\sigma) C_s \left(\frac{Q^{\text{heat}}}{\rho_0 C_P^0} \right) \quad (\text{A12})$$

575 $\overline{ws}^{\text{non-local}} = K_\lambda \gamma_s = -G(\sigma) C_s Q_s^s,$ (A13)

with the non-local terms for temperature (γ_θ) and salinity (γ_s), a dimensionless coefficient $C_s = C_* \kappa (c_s \kappa \epsilon)^{1/3}$ with a dimensionless constant $C_* = 10$, $\rho_0 = 1025 \text{ kg m}^{-3}$ the reference sea water density, C_P^0 the seawater heat capacity at constant pressure ($\text{J kg}^{-1} \text{ }^\circ\text{C}^{-1}$), Q_s the mass flux of salt ($\text{kg m}^{-2} \text{ s}^{-1}$) and the heat flux Q^{heat} (W m^{-2}) that considers penetrative shortwave radiation. See further details on the KPP scheme in Griffies et al. (2015) and Van Roekel et al. (2018).

580 Below the mixed layer, we use the PP scheme with the enhanced diffusivity parameterisation for convection, as described in section A1.

A3 TKE and IDEMIX schemes

A schematic overview of the TKE and IDEMIX schemes are depicted in Fig. A1. IDEMIX parameterises the internal wave energy (E_{iw}) in terms of a budget equation:

$$585 \quad \frac{\partial E_{iw}}{\partial t} = \nabla_h \nu_0 \tau_h \nabla_h \nu_0 E_{iw} + \frac{\partial}{\partial z} \left(c_0 \tau_v \frac{\partial c_0 E_{iw}}{\partial z} \right) - \epsilon_{iw} \quad (\text{A14})$$

with ν_0 the lateral group velocity, τ_h a lateral time scale on which lateral anisotropies are eliminated by nonlinear wave-wave interactions, c_0 the weighted average vertical group velocity, z the vertical coordinate, τ_v a time scale of on the order of days, and $\epsilon_{iw} = -\alpha E_{iw}^2$ the dissipation of internal wave energy, with α a structure function depending on the stratification (for details see (Olbers and Eden, 2013)). The first and second term on the right-hand side (RHS) parameterise the horizontal and vertical
590 propagation of internal waves, respectively. Internal wave energy is dissipated by the last term on the RHS of Eq. A14. This term acts as an energy transfer from internal wave energy to turbulent kinetic energy (see Eq. A15 below).

Internal waves are forced in IDEMIX by surface and bottom fluxes applied as boundary conditions in the second term on the RHS of Eq. A14. Currently, we use time constant fields for the energy fluxes at the surface and at the bottom (see Fig. A2), as in Eden et al. (2014). The energy flux that we use as surface boundary condition is 20 % of the wind input into the inertial band
595 of the mixed layer (Jochum et al., 2013), as determined by Rimac et al. (2013) (inertial pumping mechanism). We neglect, however, other sources exciting internal waves near the surface, for instance buoyancy plumes that overshoot the mixed layer base, vertical roll vortices of turbulent eddies, or Langmuir circulation that undulates internal waves (Czeschel and Eden, 2019). At the bottom, barotropic tides interact with the bottom roughness and convert energy to internal waves. This energy flux is prescribed from Jayne (2009), with the constraint that this energy source is not flow-aware.

600 In commonly used vertical mixing schemes, such as KPP (Large et al., 1994) or TKE (Gaspar et al., 1990), the breaking of internal waves is usually parameterised by simply assuming a constant background diffusivity (either a scalar or profile) or constant background TKE value. By using TKE with IDEMIX, the constant background diffusivity is replaced by one that is diagnosed from the internal wave energy using the Osborn-Cox relation. We use the recommended parameter set from Pollmann et al. (2017), who compared TKE coupled to IDEMIX with Argo float data in standalone ocean simulations.

605 The modified TKE equation (Eden et al., 2014) then reads:

$$\frac{d\bar{E}_{tke}}{dt} = -\partial_z(\text{fluxes}) + c_u K(\partial_z \bar{\mathbf{u}}^2) - c_b K N^2 - \epsilon_{tke} + \epsilon_{iw}, \quad (\text{A15})$$

with the dimensionless parameters c_u and c_b , which are related by $c_u = c_b R_i / R_f$. The first term on the RHS describes the redistribution of TKE in the vertical. Surface fluxes enter as boundary conditions to this term. The second term describes the vertical momentum fluxes acting on the shear of the mean flow, transferring energy from the mean flow to TKE. The third term
610 is the buoyancy term that transfers energy to the potential energy of the mean flow, thereby decreasing TKE. The dissipation of TKE (fourth term) is parameterised as $\epsilon_{tke} = \bar{E}_{tke}^{2/3} L^{-1}$ with the mixing length $L = \sqrt{2\bar{E}_{tke}/N^2}$ (Blanke and Delecluse, 1993; Eden et al., 2014). The last term on the RHS is then the new contribution from IDEMIX, which is absent when using TKE without IDEMIX.

The diffusivity is parameterised as $K = \bar{E}_{tke}^{1/2} L$ by assuming the same mixing length as for the dissipation. If TKE is used
615 alone without being combined with IDEMIX, then a background diffusivity is assumed to represent internal wave breaking
(Eden et al., 2014). When TKE is used alone without being coupled to IDEMIX, the turbulent kinetic energy is set to a
background value of $E_{\min} = 10^{-6} \text{ m}^2 \text{ s}^{-2}$. The corresponding diffusivity in this case reads $K = \sqrt{2} c_b E_{\min} / N$.

Author contributions. JJ, JvS and OG designed the experiments. DP, KL, and OG performed the simulations. OG, NB and HH have im-
plemented the KPP, TKE, and IDEMIX mixing parameterisations in MPIOM. OG prepared the manuscript with contributions from all
620 co-authors.

Competing interests. The authors declare that they have no conflict of interest.

Acknowledgements. We thank the German Computing Centre (DKRZ) for providing the computing resources. This research was funded by
the EU Horizon 2020 project PRIMAVERA (grant number 641727). This paper is a contribution to the project S2 (Improved parameterisa-
tions and numerics in climate models) of the Collaborative Research Centre TRR 181 "Energy Transfer in Atmosphere and Ocean" funded
625 by the Deutsche Forschungsgemeinschaft (DFG, German Research Foundation) - project number 274762653. JJ, OG, and KL further ac-
knowledge support by the German BMBF RACE-II project (FKZ 03F0729D). We thank Jöran März for the internal review of the manuscript
and constructive comments before submission. The Argo float data were made freely available by the International Argo Program and the
national programs that contribute to it (<http://www.argo.ucsd.edu>, <http://argo.jcommops.org>)

References

- 630 Adcroft, A. J., Hill, C., and Marshall, J.: Representation of Topography by Shaved Cells in a Height Coordinate Ocean Model, *Mon. Weather Rev.*, 125, 2293–2315, [https://doi.org/10.1175/1520-0493\(1997\)125<2293:ROTBSC>2.0.CO;2](https://doi.org/10.1175/1520-0493(1997)125<2293:ROTBSC>2.0.CO;2), 1997.
- Aldama-Campino, A. and Döös, K.: Mediterranean overflow water in the North Atlantic and its multidecadal variability, *Tellus A: Dynamic Meteorology and Oceanography*, 72:1, 1–10, <https://doi.org/10.1080/16000870.2018.1565027>, 2020.
- Axell, L. B.: Wind-driven internal waves and Langmuir circulations in a numerical ocean model of the southern Baltic Sea, *J. Geophys. Res.*, 635 107(C11), 3204, <https://doi.org/10.1029/2001JC000922>, 2002.
- Benjamini, Y. and Hochberg, Y.: Controlling the false discovery rate: a practical and powerful approach to multiple testing, *Journal of the Royal Statistical Society*, 57, 289–300, <https://doi.org/10.1111/j.2517-6161.1995.tb02031.x>, 1995.
- Berx, B., Hansen, B., Østerhus, S., Larsen, M. K., Sherwin, T., and Jochumsen, K.: Combining in situ measurements and altimetry to estimate volume, heat and salt transport variability through the Faroe-Shetland Channel, *Ocean Sci.*, 2, 127–146, <https://doi.org/10.5194/os-9-639-2013>, 2013.
- 640 Blanke, B. and Delecluse, P.: Variability of the Tropical Atlantic Ocean Simulated by a General Circulation Model with Two Different Mixed-Layer Physics, *J. Phys. Oceanogr.*, 23, 1363–1388, [https://doi.org/10.1175/1520-0485\(1993\)023<1363:VOTTAO>2.0.CO;2](https://doi.org/10.1175/1520-0485(1993)023<1363:VOTTAO>2.0.CO;2), 1993.
- Breivik, ., Mogensen, K., Bidlot, J.-R., Balmaseda, M. A., and Janssen, P. A. E. M.: Surface wave effects in the NEMO ocean model: Forced and coupled experiments, *J. Geophys. Res. Oceans*, 120, 2973–2992, <https://doi.org/10.1002/2014JC010565>, 2015.
- 645 Brüggemann, N. and Katsman, C. A.: Dynamics of Downwelling in an Eddyding Marginal Sea: Contrasting the Eulerian and the Isopycnal Perspective, *J. Phys. Oceanogr.*, 49, 3017–3035, <https://doi.org/10.1175/JPO-D-19-0090.1>, 2019.
- Campbell, E. C., Wilson, E. A., Moore, G. W. K., Riser, S. C., Brayton, C. E., Mazloff, M. R., and Talley, L. D.: Antarctic offshore polynyas linked to Southern Hemisphere climate anomalies, *Nature*, 570, 319–325, <https://doi.org/10.1038/s41586-019-1294-0>, 2019.
- Carsey, F. D.: Microwave observation of the Weddell Polynya, *Mon. Weath. Rev.*, 108, 2032–2044, [https://doi.org/10.1175/1520-0493\(1980\)108<2032:MOOTWP>2.0.CO;2](https://doi.org/10.1175/1520-0493(1980)108<2032:MOOTWP>2.0.CO;2), 1980.
- 650 Chatterjee, S., Rai, R. P., Bertino, L., Skagseth, Ø., Ravichandran, M., and Johannessen, O. M.: Role of Greenland Sea Gyre Circulation on Atlantic Water Temperature Variability in the Fram Strait, *Geophys. Res. Lett.*, 45, 8399–8406, <https://doi.org/10.1029/2018GL079174>, 2018.
- Cheon, W. G., Park, Y.-G., Toggweiler, J. R., and Lee, S.-K.: The Relationship of Weddell Polynya and Open-Ocean Deep Convection to the Southern Hemisphere Westerlies, *J. Phys. Oceanogr.*, 44 (2), 694–713, <https://doi.org/10.1175/JPO-D-13-0112.1>, 2019.
- 655 Cheon, W. G. G. and Gordon, A. L.: Open-ocean polynyas and deep convection in the Southern Ocean, *Sci. Rep.*, 9, 6935, <https://doi.org/10.1038/s41598-019-43466-2>, 2019.
- Childers, K. H., Flagg, C. N., and Rossy, T.: Direct velocity observations of volume flux between Iceland and the Shetland Islands, *J. Geophys. Res. Oceans*, 119, 5934–5944, <https://doi.org/10.1002/2014JC009946>, 2014.
- 660 Crews, L., Sundfjord, A., and Hattermann, T.: How the Yermak Pass Branch Regulates Atlantic Water inflow to the Arctic Ocean, *J. Geophys. Res. Oceans*, 124, 267–280, <https://doi.org/10.1029/2018JC014476>, 2019.
- Czeschel, L. and Eden, C.: Internal Wave Radiation through Surface Mixed Layer Turbulence, *J. Phys. Oceanogr.*, 49, 1827–1844, <https://doi.org/10.1175/JPO-D-18-0214.1>, 2019.
- Danabasoglu, G., Large, W. G., Tribbia, J. T., Gent, P. R., Briegleb, B. P., and McWilliams, J. C.: Diurnal Coupling in the Tropical Oceans of CCSM3, *J. Climate*, 19 (11), 2347–2365, <https://doi.org/10.1175/JCLI3739.1>, 2006.
- 665

- de Lavergne, C., Palter, J. B., Galbraith, E. D., Bernardello, R., and Marinov, I.: Cessation of deep convection in the open Southern Ocean under anthropogenic climate change, *Climate Change*, 4, 278–282, <https://doi.org/10.1038/nclimate2132>, 2014.
- Dee, D. P., Uppala, S. M., Simmons, A. J., Berrisford, P., Poli, P., Kobayashi, S., Andrae, U., Balmaseda, M. A., Balsamo, G., Bauer, P., Bechtold, P., Beljaars, A. C. M., van de Berg, L., Bidlot, J., Bormann, N., Delsol, C., Dragani, R., Fuentes, M., Geer, A. J., Haimberger, L., Healy, S. B., Hersbach, H., Hólm, E. V., Isaksen, I., Kåberg, P., Köhler, M., Matricardi, M., McNally, A. P., Monge-Sanz, B. M., Morcrette, J.-J., Park, B.-K., Peubey, C., de Rosnay, P., Tavolato, C., Thépaut, J.-N., and Vitart, F.: The ERA-Interim reanalysis: configuration and performance of the data assimilation system, *Q. J. R. Meteorol. Soc.*, 137, 553–597, <https://doi.org/10.1002/qj.828>, 2011.
- Dengg, J. A., Beckmann, A., and Gerdes, R.: The Warmwatersphere of the North Atlantic Ocean, chap. The Gulf Stream separation problem, pp. 253–290, Gebr. Bornträger, Berlin, 1996.
- 675 Donohue, K. A., Tracey, K. L., Watts, D. R., Chidichimo, M. P., and Chereskin, T. K.: Mean Antarctic Circumpolar Current transport measured in Drake Passage, *Geophys. Res. Lett.*, 43, 11 760–11 767, <https://doi.org/10.1002/2016GL070319>, 2016.
- Dufour, C. O., Morrison, A. K., Griffies, S. M., Frenger, I., Zanowski, H., and Winton, M.: Preconditioning of the Weddell Sea Polynya by the Ocean Mesoscale and Dense Water Overflows, *J. Climate*, 30, 7719–7737, <https://doi.org/10.1175/JCLI-D-16-0586.1>, 2017.
- DuVivier, A. K., Large, W. G., and Small, R. J.: Argo observations of the deep mixing band in the Southern Ocean: A salinity modeling challenge., *J. Geophys. Res. Oceans*, 123, 7599–7617, <https://doi.org/10.1029/2018JC014275>, 2018.
- 680 Eden, C. and Böning, C.: Sources of Eddy Kinetic Energy in the Labrador Sea, *J. Phys. Oceanogr.*, 32, 3346–3363, [https://doi.org/10.1175/1520-0485\(2002\)032<3346:SOEKEI>2.0.CO;2](https://doi.org/10.1175/1520-0485(2002)032<3346:SOEKEI>2.0.CO;2), 2002.
- Eden, C., Czeschel, L., and Olbers, D.: Toward Energetically Consistent Ocean Models, *J. Phys. Oceanogr.*, 44, 3160–3184, <https://doi.org/10.1175/JPO-D-13-0260.1>, 2014.
- 685 EUMETSAT Ocean and Sea Ice Satellite Application: Global sea ice concentration reprocessing dataset 1978-2015 (v1.2, 2015), [Online], <http://osisaf.met.no>, Norwegian and Danish Meteorological Institutes, 2015.
- Fer, I.: Weak vertical diffusion allows maintenance of cold halocline in the central Arctic, *Atmos. Ocean. Sci. Lett.*, 2(3), 148–152, <https://doi.org/10.1080/16742834.2009.11446789>, 2009.
- Fer, I., Skogseth, R., and Geyer, F.: Internal Wave and Mixing in the Marginal Ice Zone near Yermak Plateau, *J. Phys. Oceanogr.*, 40, 690 1613–1630, <https://doi.org/10.1175/2010JPO4371.1>, 2010.
- Fox-Kemper, B., Adcroft, A., Böning, C. W., Chassignet, E. P., Curchitser, E., Danabasoglu, G., Eden, C., England, M. H., Gerdes, R., Greatbatch, R. J., Griffies, S. M., Hallberg, R. W., Hanert, E., Heimbach, P., Hewitt, H. T., Hill, C. N., Komuro, Y., Legg, S., Le Sommer, J., Masina, S., Marsland, S. J., Penny, S. G., Qiao, F., Ringler, T. D., Treguier, A. M., Tsujino, H., Uotila, P., and Yeager, S. G.: Challenges and Prospects in Ocean Circulation Models, *Frontiers in Marine Science*, 6, 65, <https://doi.org/10.3389/fmars.2019.00065>, 2019.
- 695 Garrett, C.: Internal tides and ocean mixing, *Science*, 301, 1858–1859, <https://doi.org/10.1126/science.1090002>, 2003.
- Gaspar, P., Grégoris, Y., and Lefevre, J.-M.: A simple eddy kinetic energy model for simulations of the oceanic vertical mixing: Tests at station Papa and long-term upper ocean study site, *J. Geophys. Res. Oceans*, 95, 16 179–16 193, <https://doi.org/10.1029/JC095iC09p16179>, 1990.
- Gent, P. R.: A commentary on the Atlantic meridional overturning circulation stability in climate models, *Ocean Model.*, 122, 57–66, <https://doi.org/10.1016/j.ocemod.2017.12.006>, 2018.
- 700 Gent, P. R., Willebrand, J., McDougall, T. J., and McWilliams, J. C.: Parameterizing Eddy-Induced Tracer Transports in Ocean Circulation Models, *J. Phys. Oceanogr.*, 25, 463–474, [https://doi.org/10.1175/1520-0485\(1995\)025<0463:PEITTI>2.0.CO;2](https://doi.org/10.1175/1520-0485(1995)025<0463:PEITTI>2.0.CO;2), 1995.
- Georgiou, S., van der Boog, C. G., N., B., Ypma, S. L., Pietrzak, J. D., and Katsman, C. A.: On the interplay between downwelling, deep convection and mesoscale eddies in the Labrador Sea, *Ocean Modelling*, 135, 56–70, <https://doi.org/10.1016/j.ocemod.2019.02.004>, 2019.

- Good, S. A., Martin, M. J., and Rayner, N. A.: EN4: quality controlled ocean temperature and salinity profiles and monthly objective analyses with uncertainty estimates, *J. Geophys. Res.*, 118, 6704–6716, <https://doi.org/10.1002/2013JC009067>, 2013.
- 705
- Gordon, A. L.: Deep Antarctic Convection West of Maud Rise, *J. Phys. Oceanogr.*, 8, 600–612, [https://doi.org/10.1175/1520-0485\(1978\)008<0600:DACWOM>2.0.CO;2](https://doi.org/10.1175/1520-0485(1978)008<0600:DACWOM>2.0.CO;2), 1978.
- Gordon, A. L.: Southern Ocean polynya, *Nature Clim. Change*, 4, 249–250, <https://doi.org/10.1038/nclimate2179>, 2014.
- Griffies, S. M., Levy, M., Adcroft, A. J., Danabasoglu, R., Hallberg, R. W., Jacobsen, D., Large, W., and Ringler, T. D.: Theory and numerics of the Community Ocean Vertical Mixing (CVMix) Project, Tech. rep., NOAA/Geophysical Fluid Dynamics Laboratory, Princeton, NJ, <https://github.com/CVMix/CVMix-description>, 2015.
- 710
- Gutjahr, O., Putrasahan, D., Lohmann, K., Jungclaus, J. H., von Storch, J.-S., Brüggemann, N., Haak, H., and Stössel, A.: Max Planck Institute Earth System Model (MPI-ESM1.2) for the High-Resolution Model Intercomparison Project (HighResMIP), *Geosci. Model Dev.*, 12, 3241–3281, <https://doi.org/10.5194/gmd-12-3241-2019>, 2019.
- 715
- Haarsma, R. J., Roberts, M. J., Vidale, P. L., Senior, C. A., Bellucci, A., Bao, Q., Chang, P., Corti, S., Fučkar, N. S., Guemas, V., von Hardenberg, J., Hazeleger, W., Kodama, C., Koenigk, T., Leung, L. R., Lu, J., Luo, J.-J., Mao, J., Mizielinski, M. S., Mizuta, R., Nobre, P., Satoh, M., Scoccimarro, E., Semmler, T., Small, J., and von Storch, J.-S.: High Resolution Model Intercomparison Project (HighResMIP v1.0) for CMIP6, *Geosci. Model Dev.*, 9, 4185–4208, <https://doi.org/10.5194/gmd-9-4185-2016>, 2016.
- Hagemann, S. and Gates, L. D.: Improving a subgrid runoff parameterization scheme for climate models by the use of a high resolution data derived from satellite observations, *Climate Dyn.*, 21, 349–359, <https://doi.org/10.1007/s00382-003-0349-x>, 2003.
- 720
- Hansen, B., Østerhus, S., Quadfasel, D., and Turrell, W.: Already the day after tomorrow?, *Science*, 304, 953–954, <https://doi.org/10.1126/science.1100085>, 2004.
- Hansen, B., Larsen, K. M. H., Hátún, H., Kristiansen, R., Mortensen, E., and Østerhus, S.: Transport of volume, heat, and salt towards the Arctic in the Faroe Current 1993–2013, *Ocean Sci.*, 11, 743–757, <https://doi.org/10.5194/os-11-743-2015>, 2015.
- 725
- Hansen, B., Húsgarð, K. M., Hátún, H., and Østerhus, S.: A stable Faroe Bank Channel overflow 1995–2015, *Ocean Sci.*, 12, 1205–1220, <https://doi.org/10.5194/os-12-1205-2016>, 2016.
- Hansen, B., Poulsen, T., Larsen, K. M. H., Hátún, H., Østerhus, S., Darelius, E., Berx, B., Quadfasel, D., and Jochumsen, K.: Atlantic water flow through the Faroese Channel, *Ocean Sci.*, 13, 873–888, <https://doi.org/10.5194/os-13-873-2017>, 2017.
- Heuzé, C., Ridley, J. K., Calvert, D., Stevens, D. P., and Heywood, K. J.: Increasing vertical mixing to reduce Southern Ocean deep convection in NEMO3.4, *Geoscientific Model Development*, 8, 3119–3130, <https://doi.org/10.5194/gmd-8-3119-2015>, 2015.
- 730
- Holloway, G., Dupont, F., Golubeva, E., Haekkinen, S., Hunke, E., Jin, M., Karcher, M., Kauker, F., Maltrud, M., Maqueda, M. A. M., Maslowski, W., Platov, G., Stark, D., Steele, M., Suzuki, T., Wang, J., and Zhang, J.: Water properties and circulation in Arctic Ocean models, *Geophys. Res. Oceans*, 112, C04S03, <https://doi.org/10.1029/2006JC003642>, 2007.
- Holte, J., Talley, L. D., Gilson, J., and Roemmich, D.: An Argo mixed layer climatology and database, *Geophys. Res. Lett.*, 44, 5618–5626, <https://doi.org/10.1002/2017GL073426>, 2017.
- 735
- Jayne, S. R.: The impact of abyssal mixing parameterizations in an ocean general circulation model, *J. Phys. Oceanogr.*, 39, 1756–1775, <https://doi.org/10.1175/2009JPO4085.1>, 2009.
- Jena, B., Ravichandran, M., and Turner, J.: Recent Reoccurrence of Large Open-Ocean Polynya on the Maud Rise Seamount, *Geophys. Res. Lett.*, 46, 4320–4329, <https://doi.org/10.1029/2018GL081482>, 2019.
- 740
- Jochum, M., Briegleb, B. P., Danabasoglu, G., Large, W. G., Norton, N. J., Jayne, S. R., Alford, M. H., and Bryan, F. O.: The impact of oceanic near-inertial waves on climate, *J. Climate*, 26, 2833–2844, <https://doi.org/10.1175/JCLI-D-12-00181.1>, 2013.

- Jochumsen, K., Quadfasel, D., Valdimarsson, H., and Jónsson, S.: Variability of the Denmark Strait overflow: Moored time series from 1996–2011, *J. Geophys. Res.*, 117, C12 003, <https://doi.org/10.1029/2012JC008244>, 2012.
- 745 Jochumsen, K., Moritz, M., Nunes, N., Quadfasel, D., Larsen, K. M. H., Hansen, B., Valdimarsson, H., and Jonsson, S.: Revised transport estimates of the Denmark Strait overflow, *J. Geophys. Res.*, 122, 3434–3450, 2017.
- Jones, D. C., Meijers, J. S., Shuckburgh, E., Sallée, J.-B., Haynes, P., McAufield, E. K., and Mazloff, M. R.: How does Subantarctic Mode Water ventilate the Southern Hemisphere subtropics?, *J. Geophys. Res. Oceans*, 121, 6558–6582, <https://doi.org/10.1002/2016JC011680>, 2016.
- 750 Jungclaus, J. H., Fischer, N., Haak, H., Lohmann, K., Marotzke, J., Matei, D., Mikolajewicz, U., Notz, D., and von Storch, J. S.: Characteristics of the ocean simulations in the Max Planck Institute Ocean Model (MPIOM), the ocean component of the MPI-Earth system model, *J. Adv. Model. Earth Syst.*, 5, 422–446, <https://doi.org/10.1002/jame.20023>, 2013.
- Katsman, C. A., Drijfhout, S. S., Dijkstra, H. A., and Spall, M. A.: Sinking of Dense North Atlantic Waters in a Global Ocean Model: Location and Controls, *J. Geophys. Res. Oceans*, 123, 3563–3576, <https://doi.org/10.1029/2017JC013329>, 2018.
- 755 Kim, S. Y., Lee, H. J., Park, J.-H., and Kim, Y. H.: Effects of Reduced Vertical Mixing Under Sea Ice on Atlantic Meridional Overturning Circulation (AMOC) in a Global Ice-Ocean Model, *Ocean Sci. J.*, 50 (2), 155–161, <https://doi.org/10.1007/s12601-015-0012-6>, 2015.
- Kjellsson, J., Holland, P. R., Marshall, G. J., Mathiot, P., Aksenov, Y., Coward, A. C., Bacon, S., Megann, A. P., and Ridley, J.: Model sensitivity of the Weddell and Ross seas, Antarctica, to vertical mixing and freshwater forcing, *Ocean Modelling*, 94, 141–152, <https://doi.org/10.1016/j.ocemod.2015.08.003>, 2015.
- 760 Kurtakoti, P., Veneziani, M., Stössel, A., and Weijer, W.: Preconditioning and Formation of Maud Rise Polynyas in a High-Resolution Earth System Model, *J. Climate*, 31, 9659–9678, <https://doi.org/10.1175/JCLI-D-18-0392.1>, 2018.
- Large, W. G., McWilliams, J. C., and Doney, S. C.: Oceanic vertical mixing: A review and a model with a nonlocal boundary layer parameterization, *Rev. Geophys.*, 21, 363–403, <https://doi.org/10.1029/94RG01872>, 1994.
- Li, Q. and Fox-Kemper, B.: Assessing the effects of Langmuir turbulence on the entrainment buoyancy flux in the ocean surface boundary layer, *J. Phys. Oceanogr.*, 47, 2863–2886, <https://doi.org/10.1175/JPO-D-17-0085.1>, 2017.
- 765 Li, Q. and Lee, S.: A mechanism of mixed-layer formation in the Indo-western Pacific Southern Ocean: Preconditioning by an eddydriven jet-scale overturning circulation, *J. Phys. Oceanogr.*, 47, 2775–2772, <https://doi.org/10.1175/JPO-D-17-0006.1>, 2017.
- Li, Q., Reichl, B. G., Fox-Kemper, B., Adcroft, A. J., Belcher, S. E., Danabasoglu, G., Grant, A. L. M., Griffies, S. M., Hallberg, R., Hara, T., Harcourt, R. R., Kukulka, T., Large, W. G., McWilliams, J. C., Pearson, B., Sullivan, P. P., Van Roekel, L., Wang, P., and Zheng, Z.: Comparing Ocean Surface Boundary Vertical Mixing Schemes Including Langmuir Turbulence, *Journal of Advances in Modeling Earth Systems*, 11, <https://doi.org/10.1029/2019MS001810>, 2019.
- 770 Liang, X. and Losch, M.: On the effects of increased vertical mixing on the Arctic Ocean and sea ice, *J. Geophys. Res. Oceans*, 26, 2833–2844, <https://doi.org/10.1029/2018JC014303>, 2018.
- Lozier, M. S. and Sindlinger, L.: On the source of Mediterranean Overflow Water property changes, *J. Phys. Oceanogr.*, 39, 1800–1817, <https://doi.org/10.1175/2009JPO4109.1>, 2008.
- 775 Marsland, S. J., Haak, H., Jungclaus, J. H., Latif, M., and Röske, F.: The Max Planck Institute global ocean/sea ice model with orthogonal curvilinear coordinates, *Ocean Model.*, 5, 91–127, [https://doi.org/10.1016/S1463-5003\(02\)00015-X](https://doi.org/10.1016/S1463-5003(02)00015-X), 2003.
- Mauritsen, T., Stevens, B., Roeckner, E., Crueger, T., Esch, M., Giorgetta, M., Haak, H., Jungclaus, J. H., Klocke, D., Matei, D., Mikolajewicz, U., Notz, D., Pincus, R., Schmidt, H., and Tomassini, L.: Tuning the climate of a global model, *J. Adv. Model. Earth Syst.*, 4(3), M00A01, <https://doi.org/10.1029/2012MS000154>, 2012.

- 780 Mauritsen, T., Bader, J., Becker, T., Behrens, J., Bittner, M., Brokopf, R., Brovkin, V., Claussen, M., Crueger, T., Esch, M., Fast, I., Fiedler, S., Fläschner, D., Gayler, V., Giorgetta, M., Haak, M., Hagemann, S., Hedemann, C., Hohenegger, C., Ilyina, T., Jahns, T., Jimenéz-de-la Cuesta, D., Jungclaus, J., Kleinen, T., Kloster, S., Kracher, D., Kinne, S., Kleberg, S., Lasslop, G., Kornblueh, L., Marotzke, J., Matei, D., Meraner, K., Mikilajewicz, U., Modali, K., Möbis, B., Müller, W. A., Nabel, J. E. M. S., Nam, C. C. W., Notz, D., Nyawira, S.-S., Paulsen, H., Peters, K., Pincus, R., Pohlmann, H., Pongratz, J., Popp, M., Raddatz, T. J., Rast, S., Redler, R., Reick, C. H., Rohrschneider, T., Schemann, V., Schmidt, H., Schnur, R., Schulzweida, S., Six, K. D., Stein, L., Stemmler, I., Stevens, B., von Storch, J.-S., Tian, F., Voigt, A., Vrese, P., Wienders, K.-H., Wilkenskjeld, S., Winkler, A., and Roeckner, E.: Developments in the MPI-M Earth System Model version 1.2 (MPI-ESM1.2) and Its Response to Increasing CO₂, *Journal of Advances in Modeling Earth Systems*, 11, 998–1038, <https://doi.org/10.1029/2018MS001400>, 2019.
- McCartney, M. S.: A Voyage of Discovery: George Deacon 70th Anniversary Volume, chap. Subantarctic Mode Water, pp. 103–119, Supplement to Deep-Sea Research, Pergamon Press, Oxford, 1977.
- 790 McCartney, M. S. and Mauritsen, C.: On the origin of the warm inflow to the Nordic Seas, *Prog. Oceanogr.*, 51, 125–214, [https://doi.org/10.1016/S0079-6611\(01\)00084-2](https://doi.org/10.1016/S0079-6611(01)00084-2), 2001.
- McWilliams, J. C., Sullivan, P. P., and Moeng, C.-H.: Langmuir turbulence in the ocean, *J. Fluid Mech.*, 334, 1–30, <https://doi.org/10.1017/S0022112096004375>, 1997.
- 795 Mellor, G. and Yamada, T.: Development of a turbulent closure model for geophysical fluid problems, *Rev. Geophys.*, 20, 851–875, <https://doi.org/10.1029/RG020i004p00851>, 1982.
- Milinski, S., Bader, J., Haak, H., Siogco, A. C., and Jungclaus, J. H.: High atmospheric horizontal resolution eliminates the wind-driven coastal warm bias in the southeastern tropical Atlantic, *Geophys. Res. Lett.*, 43, 10455–10462, <https://doi.org/10.1002/2016GL070530>, 2016GL070530, 2016.
- 800 Muilwijk, M., Ilicak, M., Cornish, S. B., Danilov, S., Gelderloos, R., Gerdes, R., Haid, V., Haine, T. W. N., Johnson, H. L., Kostov, Y., Kovács, T., Lique, C., Marson, J. M., Myers, P. G., Scott, J., Smedsrud, L. H., Talandier, C., and Wang, Q.: Arctic Ocean Response to Greenland Sea Wind Anomalies in a Suite of Model Simulations, *Journal of Geophysical Research: Oceans*, 124, 6286–6322, <https://doi.org/10.1029/2019JC015101>, 2019.
- Müller, W. A., Jungclaus, J. H., Mauritsen, T., Baehr, J., Bittner, M., Budich, R., Bunzel, F., Esch, M., Ghosh, R., Haak, H., Ilyina, T., 805 Kleine, T., Kornblueh, L., Li, H., Modali, K., Notz, D., Pohlmann, H., Roeckner, E., Stemmler, I., Tian, F., and Marotzke, J.: A higher-resolution version of the Max Planck Institute Earth System Model (MPI-ESM 1.2-HR), *J. Adv. Model. Earth Syst.*, 10, 1383–1413, <https://doi.org/10.1029/2017MS001217>, 2018.
- Naughten, K., Meissner, K. J., Galton-Fenzi, B. K., England, M. H., Timmermann, R., Hellmer, H. H., Hattermann, T., and Debernard, J. B.: Intercomparison of Antarctic ice-shelf, ocean, and sea-ice interactions simulated by MetROMS-iceshelf and FESOM 1.4, *Geosci. Model. Dev.*, 11, 1257–1292, <https://doi.org/10.5194/gmd-11-1257-2018>, 2018.
- 810 Nielsen, S. B., Jochum, M., Eden, C., and Nuterman, R.: An energetically consistent vertical mixing parameterization in CCSM4, *Ocean Model.*, 127, 46–54, <https://doi.org/10.1016/j.ocemod.2018.03.002>, 2018.
- Nielsen, S. B., Jochum, M., Pedro, J. B., Eden, C., and Nuterman, R.: Two-Timescale Carbon Cycle Response to an AMOC Collapse, *Paleoceanography and Paleoclimatology*, 34 (4), 511–523, <https://doi.org/10.1029/2018PA003481>, 2019.
- 815 Notz, D., Haumann, F. A., Haak, H., Jungclaus, J. H., and Marotzke, J.: Arctic sea-ice evolution as modeled by Max Planck Institute for Meteorology’s Earth system model, *J. Adv. Model. Earth Syst.*, 5, 173–194, <https://doi.org/10.1002/jame.20016>, 2013.

- Olbers, D. and Eden, C.: A Global Model for the Diapycnal Diffusivity Induced by Internal Gravity Waves, *J. Phys. Oceanogr.*, 43, 1759–1779, <https://doi.org/10.1175/JPO-D-12-0207.1>, 2013.
- Orsi, A. H., Nowlin Jr., W. D., and Whitworth III, T.: On the circulation and stratification of the Weddell Gyre, *Deep-Sea Res.*, 40, 169–203, [https://doi.org/10.1016/0967-0637\(93\)90060-G](https://doi.org/10.1016/0967-0637(93)90060-G), 1993.
- 820 Pacanowski, R. C. and Philander, S. G. H.: Parameterization of Vertical Mixing in Numerical Models of Tropical Oceans, *J. Phys. Oceanogr.*, 11, 1443–1451, [https://doi.org/10.1175/1520-0485\(1981\)011<1443:POVMIN>2.0.CO;2](https://doi.org/10.1175/1520-0485(1981)011<1443:POVMIN>2.0.CO;2), 1981.
- Pickart, R. S., Spall, M. A., Ribergaard, M. H., Moore, G. W. K., and Milliff, R. F.: Deep convection in the Irminger Sea forced by the Greenland tip jet, *Nature*, 424, 152–156, <https://doi.org/10.1038/nature01729>, 2003.
- 825 Pollmann, F., Eden, C., and Olbers, D.: Evaluating the Global Internal Wave Model IDEMIX Using Finestructure Methods, *J. Phys. Oceanogr.*, 47, 2267–2289, <https://doi.org/10.1175/JPO-D-16-0204.1>, 2017.
- Putrasahan, D. A., Lohmann, K., von Storch, J. S., Jungclaus, J. H., Haak, H., and Gutjahr, O.: Surface flux drivers for the slowdown of the Atlantic Meridional Overturning Circulation in a high-resolution global coupled climate model, *J. Adv. Model. Earth Syst.*, 11, 1349–1363, <https://doi.org/10.1029/2018MS001447>, 2019.
- 830 Rainville, L. and Winsor, P.: Mixing across the Arctic Ocean: Microstructure observations during the Beringia 2005 Expedition, *Geophys. Res. Lett.*, 35, L08 606, <https://doi.org/10.1029/2008GL033532>, 2008.
- Rainville, L. and Woodgate, R.: Observations of internal wave generation in the seasonally ice-free Arctic, *Geophys. Res. Lett.*, 36, L23 604, <https://doi.org/10.1029/2009GL041291>, 2009.
- Randall, D. A., Wood, R. A., Bony, S., Colman, R., Fichefet, T., Fyfe, J., Kattsov, V., Pitman, A., Shukla, J., Srinivasan, J., Stouffer, R. J., Sumi, A., and Taylor, K. E.: *Climate Change 2007: The Physical Science Basis. Contribution of Working Group I to the Fourth Assessment Report of the Intergovernmental Panel on Climate Change*, chap. Climate Models and Their Evaluation, Cambridge University Press, Cambridge, United Kingdom and New York, NY, USA, 2007.
- 835 Redi, M. H.: Oceanic Isopycnal Mixing by Coordinate Rotation, *Journal of Physical Oceanography*, 12, 1154–1158, [https://doi.org/10.1175/1520-0485\(1982\)012<1154:OIMBCR>2.0.CO;2](https://doi.org/10.1175/1520-0485(1982)012<1154:OIMBCR>2.0.CO;2), 1982.
- 840 Reid, J. L.: On the contribution of the Mediterranean Sea outflow to the Norwegian-Greenland Sea, *Deep-Sea Res.*, 26A, 1199–1223, [https://doi.org/10.1016/0198-0149\(79\)90064-5](https://doi.org/10.1016/0198-0149(79)90064-5), 1979.
- Rimac, A., von Storch, J.-S., Eden, C., and Haak, H.: The influence of high-resolution wind stress field on the power input to near-inertial motions in the ocean, *Geophys. Res. Lett.*, 40, 4882–4886, <https://doi.org/10.1002/grl.50929>, 2013.
- Rippeth, T. P., Lincoln, B. J., Lenn, Y.-D., Green, J. A. M., Sundfjord, A., and Bacon, S.: Tide-mediated warming of Arctic halocline by Atlantic heat fluxes over rough topography, *Nat. Geosci.*, 8, 191–194, <https://doi.org/10.1038/ngeo2350>, 2015.
- 845 Rippeth, T. P., Vlasenko, V., Stashchuk, N., Scanell, B. D., Green, J. A. M., Lincoln, B. J., and Bacon, S.: Tidal conversion and mixing poleward of the critical latitude (an Arctic case study), *Geophys. Res. Lett.*, 44, 12 349–12 357, <https://doi.org/10.1002/2017GL075310>, 2017.
- Robertson, R. and Dong, C.: An evaluation of the performance of vertical mixing parameterizations for tidal mixing in the Regional Ocean Model System (ROMS), *Geosci. Lett.*, 6, 1–18, <https://doi.org/10.1186/s40562-019-0146-y>, 2019.
- 850 Rossby, T. and Flagg, C. N.: Direct measurements of volume flux in the Faroe-Shetland Channel and over the Iceland-Faroe Ridge, *Geophys. Res. Lett.*, 39, L07 602, <https://doi.org/10.1029/2012GL051269>, 2012.
- Sabine, C. L., Freely, R. A., Gruber, N., Key, R. M., Lee, K., and Bullister, J. L.: The oceanic sink for anthropogenic CO₂, *Science*, 305 (5682), 367–371, <https://doi.org/10.1126/science.1097403>, 2004.

- 855 Sallée, J.-B., Shuckburgh, E., Bruneau, N., Meijers, A. J. S., Bracegirdle, T. J., and Wang, Z.: Assessment of Southern Ocean mixed-layer depths in CMIP5 models: Historical bias and forcing response, *J. Geophys. Res. Oceans*, 118, 1845–1862, <https://doi.org/10.1002/jgrc.20157>, 2013.
- Sarmiento, J., Gruber, N., Brzezinski, M., and Dunne, J.: High-latitude controls of thermocline nutrients and low latitude biological productivity, *Nature*, 427, 56–60, <https://doi.org/10.1038/nature02127>, 2004.
- 860 Sayol, J.-M., Dijkstra, H., and Katsman, C.: Seasonal and regional variations of sinking in the subpolar North Atlantic from a high-resolution ocean model, *Ocean Sci.*, 15, 1033–1053, <https://doi.org/10.5194/os-15-1033-2019>, 2019.
- Schweiger, A., Lindsay, R., Zhang, J., Steele, M., Stern, H., and Kwok, R.: Uncertainty in modelled Arctic sea ice volume, *J. Geophys. Res. Oceans*, 116, D06, <https://doi.org/10.1029/2011JC007084>, 2011.
- Sein, D. V., Koldunov, N. V., Danilov, S., Sidorenko, D., Wekerle, C., Cabos, W., Rackow, T., Scholz, P., Semmler, T., Wang, Q., and Jung, T.: The relative influence of atmospheric and oceanic model resolution on the circulation of the North Atlantic Ocean in a coupled climate model, *J. Adv. Model. Earth Syst.*, 10, 2026–2041, <https://doi.org/10.1029/2018MS001327>, 2018.
- 865 Shu, Q., Wang, Q., Su, J., Li, X., and Fangli, Q.: Assessment of the Atlantic water layer in the Arctic Ocean in CMIP5 climate models, *Clim. Dyn.*, 53(9), 5279–5291, <https://doi.org/10.1007/s00382-019-04870-6>, 2019.
- Simmons, H. L., Jayne, S. R., St. Laurent, L. C., and Weaver, A. J.: Tidally driven mixing in a numerical model of the ocean general circulation, *Ocean Modelling*, 6, 245–263, [https://doi.org/10.1016/S1463-5003\(03\)00011-8](https://doi.org/10.1016/S1463-5003(03)00011-8), 2004.
- 870 Sloyan, B. and Rintoul, S.: Circulation, renewal, and modification of Antarctic mode and intermediate water, *J. Phys. Oceanogr.*, 31, 1005–1030, [https://doi.org/10.1175/1520-0485\(2001\)031<1005:CRAMOA>2.0.CO;2](https://doi.org/10.1175/1520-0485(2001)031<1005:CRAMOA>2.0.CO;2), 2001.
- Stevens, B., Giorgetta, M., Esch, M., Mauritsen, T., Crueger, T., Rast, S., Salzmann, M., Schmidt, H., Bader, J., Block, K., Brokopf, R., Fast, I., Kinne, S., Kornblueh, L., Lohmann, U., Pincus, R., Reichler, T., and Roeckner, E.: Atmospheric component of the MPI-M Earth System Model: ECHAM6, *J. Adv. Model. Earth Syst.*, 5, 146–172, <https://doi.org/10.1002/jame.20015>, 2013.
- 875 Stössel, A., Notz, D., Haumann, F. A., Haak, H., Jungclaus, J., and Mikolajewicz, U.: Controlling high-latitude Southern Ocean convection in climate models, *Ocean Model.*, 86, 58–75, <https://doi.org/10.1016/j.ocemod.2014.11.008>, 2015.
- Timmermann, R. and Beckmann, A.: Parameterization of vertical mixing in the Weddell Sea, *Ocean Model.*, 6, 83–100, [https://doi.org/10.1016/S1463-5003\(02\)00061-6](https://doi.org/10.1016/S1463-5003(02)00061-6), 2004.
- 880 Våge, K., Pickart, R., Sarafanov, A., Knutsen, Ø., Mercier, H., Lherminier, P., van Aken, H. M., Meincke, J., Quadfasel, D., and Bacon, S.: The Irminger Gyre: circulation, convection, and interannual variability, *Deep-Sea Res. I*, 58, 590–614, <https://doi.org/10.1016/j.dsr.2011.03.001>, 2011.
- Valcke, S.: The OASIS3 coupler: a European climate modelling community software, *Geosci. Model. Dev.*, 6, 373–388, <https://doi.org/10.5194/gmd-6-373-2013>, 2013.
- 885 Van Roekel, L., Adcroft, A. J., Danabasoglu, G., Griffies, S. M., Kauffman, B., Large, W., Levy, M., Reichl, B. G., Ringler, T., and Schmidt, M.: The KPP Boundary Layer Scheme for the Ocean: Revisiting Its Formulation and Benchmarking One-Dimensional Simulations Relative to LES, *Adv. Model. Earth Syst.*, 10, 2647–2685, <https://doi.org/10.1029/2018MS001336>, 2018.
- Wang, Q., Danilov, S., Sidorenko, D., Timmermann, R., Wekerle, C., Wang, X., Jung, T., and Schröter, J.: The Finite Element Sea Ice-Ocean Model FESOM v.1.4: formulation of an ocean general circulation model, *Geosci. Model. Dev.*, 7, 663–693, <https://doi.org/10.5194/gmd-7-663-2014>, 2014.
- 890 Wang, Q., Wekerle, C., Danilov, S., Wang, X., and Jung, T.: A 4.5 km resolution Arctic Ocean simulation with the global multi-resolution model FESOM1.4, *Geosci. Model. Dev.*, 11, 1229–1255, <https://doi.org/10.5194/gmd-11-1229-2018>, 2018.

- Wekerle, C., Wang, Q., von Appen, W.-J., Danilov, S., Schourup-Kristensen, V., and Jung, T.: Eddy-resolving simulation of the Atlantic Water circulation in the Fram Strait with focus on the seasonal cycle, *J. Geophys. Res. Oceans*, 122, 8385–8405, 895 <https://doi.org/10.1002/2017JC012974>, 2017.
- Wolff, J. O., Maier-Reimer, E., and Legutke, S.: The Hamburg Ocean Primitive Equation Model HOPE, Tech. Rep. 13, German Climate Computer Center (DKRZ), 1997.
- Zhang, J. and Rothrock, D. A.: Modeling Global Sea Ice with a Thickness and Enthalpy Distribution Model in Generalized Curvilinear Coordinates, *Mon. Weather Rev.*, 131, 845–861, [https://doi.org/10.1175/1520-0493\(2003\)131<0845:MGSIWA>2.0.CO;2](https://doi.org/10.1175/1520-0493(2003)131<0845:MGSIWA>2.0.CO;2), 2003.
- 900 Zhang, J. and Steele, M.: Effect of vertical mixing on the Atlantic Water layer circulation in the Arctic Ocean, *Geophys. Res. Oceans*, 112, C04S04, <https://doi.org/10.1029/2006JC003732>, 2007.

Table 1. Overview of the 100 year long control simulations conducted with MPI-ESM1.2-HR. All simulations use a T127 (about 100 km) resolution in the atmosphere and a resolution of 0.4° (about 40 km) on a tripolar grid (TP04) in the ocean. The number of vertical levels are 95 in the atmosphere and 40 in the ocean, respectively. All models were analysed for the model years 80–100.

Experiment	Ocean mixing scheme	Description	Reference
HR _{pp}	PP	reference simulation	(Pacanowski and Philander, 1981)
HR _{kpp}	KPP	uses PP scheme below mixed layer	(Large et al., 1994; Griffies et al., 2015)
HR _{tke}	TKE	background diffusivity $K = \sqrt{2}E_{\min}/N$ with $E_{\min} = 10^{-6} \text{ m}^2\text{s}^{-2}$	(Gaspar et al., 1990)
HR _{ide}	TKE + IDEMIX	$E_{\min} = 0 \text{ m}^2\text{s}^{-2}$; prognostic simulation of internal gravity waves	(Eden et al., 2014)

Table 2. Time-averaged volume transport ($1 \text{ Sv} = 10^6 \text{ m}^3 \text{ s}^{-1}$) of Denmark Strait Overflow Water (DSOW), Faroe Bank Channel (FBC) and Faroe-Shetland Channel (FSC) overflow from simulations with MPI-ESM1.2-HR. Hansen et al. (2017) note that measurements by Rossby and Flagg (2012) and Childers et al. (2014) include a closed circulation on the Faroe Shelf (0.6 Sv) and flow on the Scottish Shelf, which are not included in measurements by Berx et al. (2013) and Hansen et al. (2015). A standard deviation based on annual averages is given for the simulations.

Observations/Experiment	DSOW	FBC	FSC
Jochumsen et al. (2017)	-3.2 ± 0.5	-	-
Jochumsen et al. (2012)	-3.4	-	-
Hansen et al. (2016)	-	2.2	-
Berx et al. (2013); Hansen et al. (2015)	-	-	2.7
Rossby and Flagg (2012)	-	-	0.9
Childers et al. (2014)	-	-	1.5
HR_{pp}	-1.8 ± 0.2	1.8 ± 0.1	3.2 ± 0.4
HR_{kpp}	-2.1 ± 0.4	1.8 ± 0.2	3.3 ± 0.3
HR_{tke}	-2.2 ± 0.3	1.9 ± 0.1	3.5 ± 0.2
HR_{ide}	-2.1 ± 0.3	1.7 ± 0.1	3.3 ± 0.3

Table 3. Time-averaged volume transport ($1 \text{ Sv} = 10^6 \text{ m}^3 \text{ s}^{-1}$) of the Antarctic Circumpolar Current (ACC) through Drake Passage from observations and simulations with MPI-ESM1.2-HR.

Experiment	Mean	Standard deviation
Donohue et al. (2016)	173.3 ± 10.7	-
HR _{pp}	161.41	2.14
HR _{kpp}	191.97	2.99
HR _{tke}	174.31	2.63
HR _{ide}	163.54	4.39

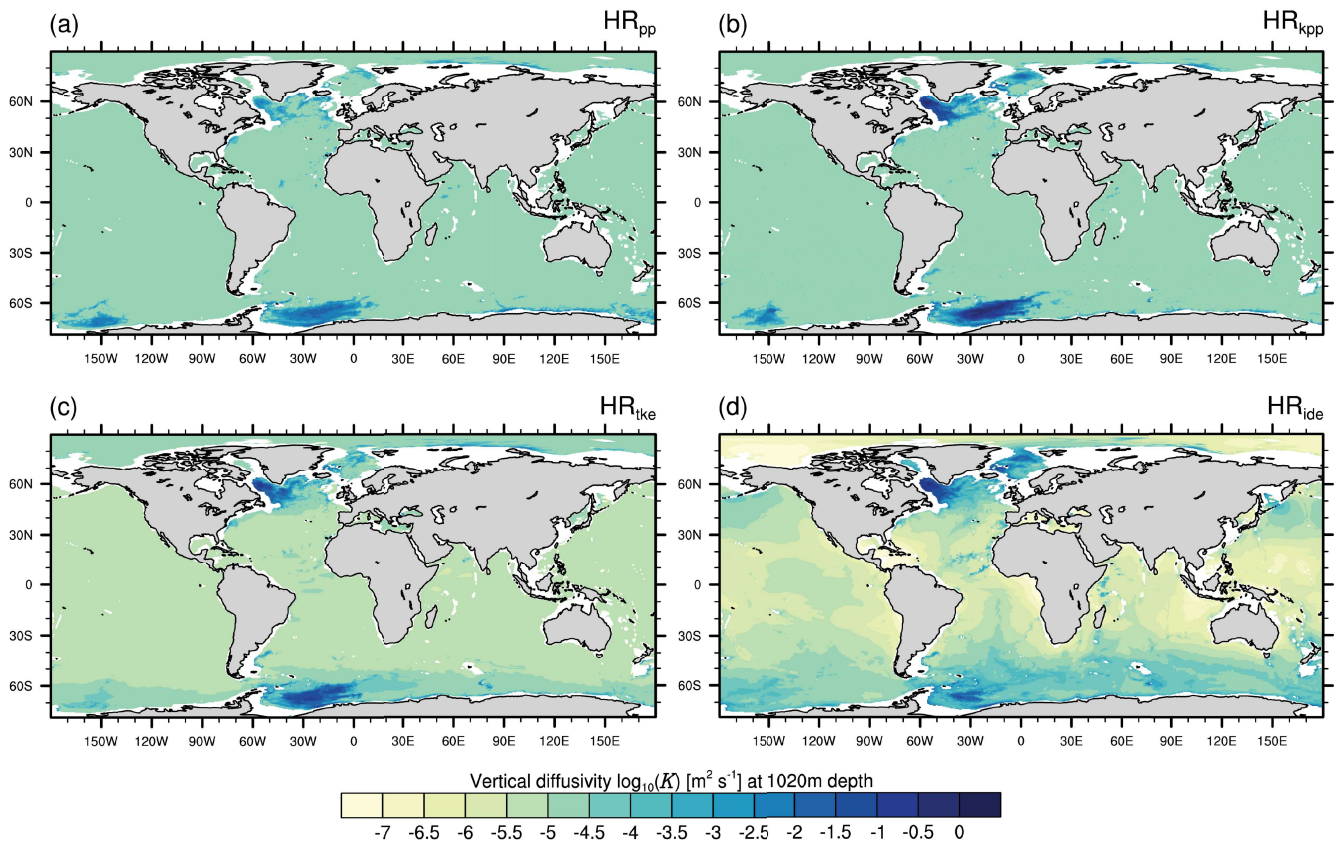


Figure 1. Time-averaged vertical diffusivity $\log_{10}(K)$ ($\text{m}^2 \text{s}^{-1}$) at a depth of 1020 m in the MPI-ESM1.2-HR simulations for (a) HR_{pp} , (b) HR_{kpp} , (c) HR_{tke} , and (d) HR_{ide} .

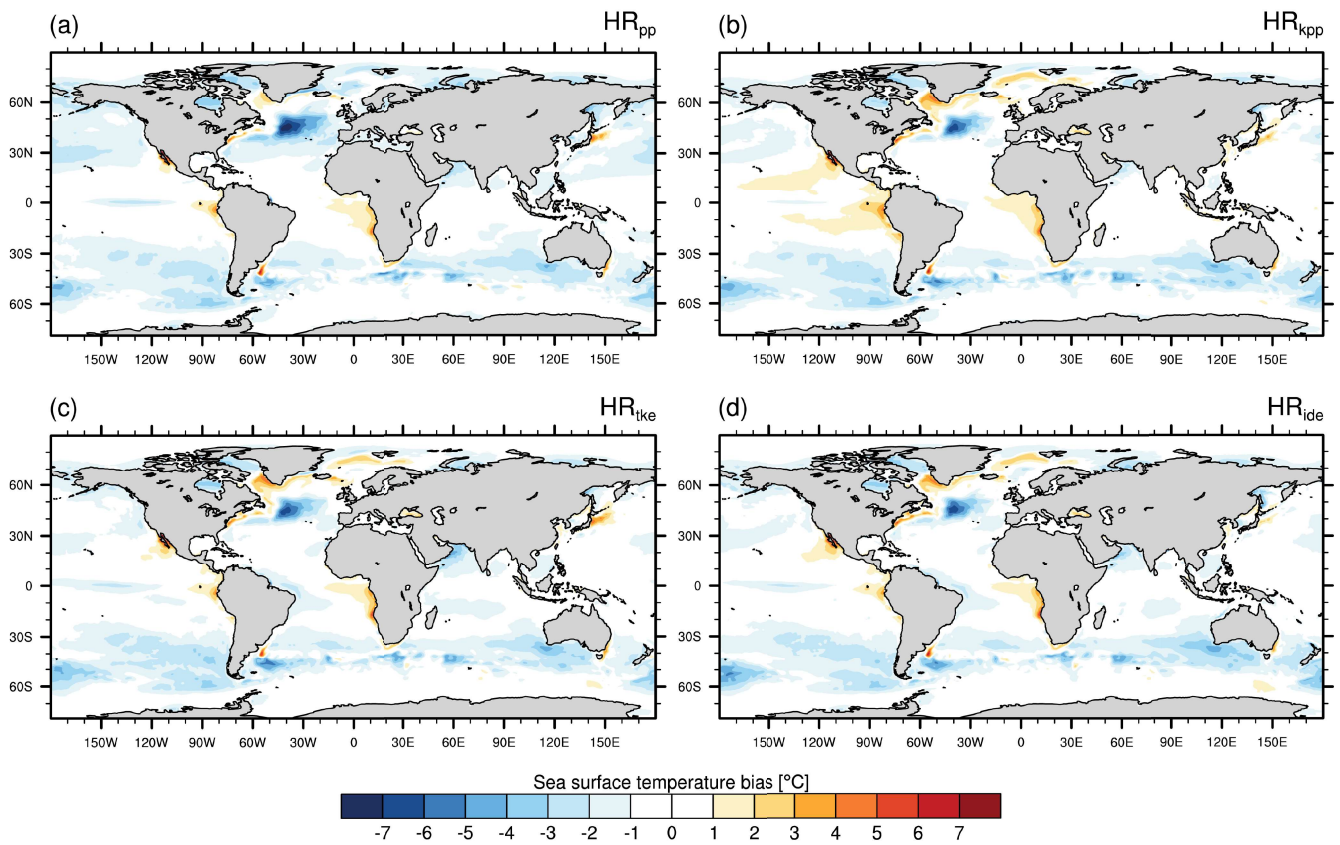


Figure 2. Time-averaged sea surface temperature bias of MPI-ESM1.2-HR minus EN4 (1945-1955) for (a) HR_{pp} , (b) HR_{kpp} , (c) HR_{tke} , and (d) HR_{ide} .

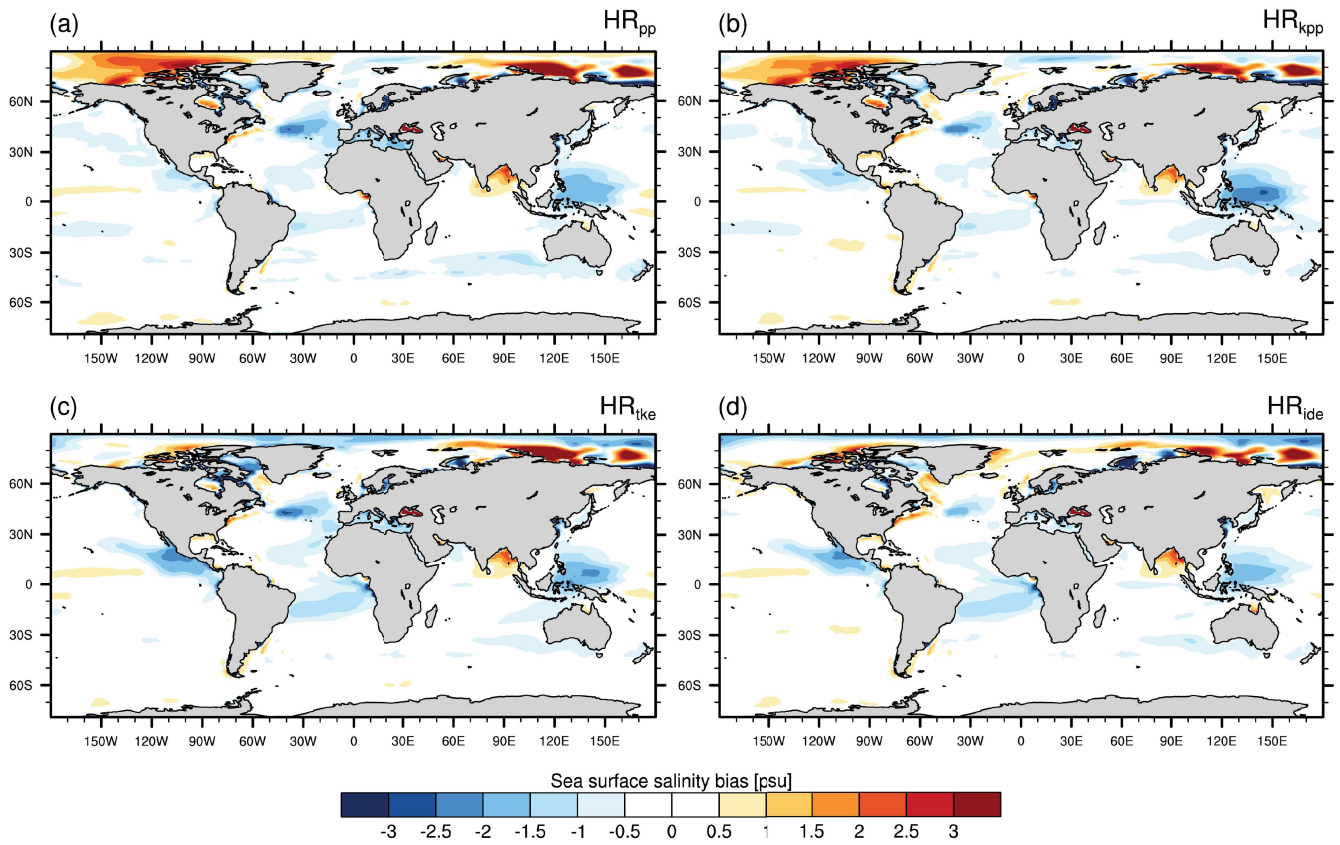


Figure 3. Time-averaged sea surface salinity bias of MPI-ESM1.2-HR minus EN4 (1945-1955) for (a) HR_{pp} , (b) HR_{kpp} , (c) HR_{tke} , and (d) HR_{ide} .

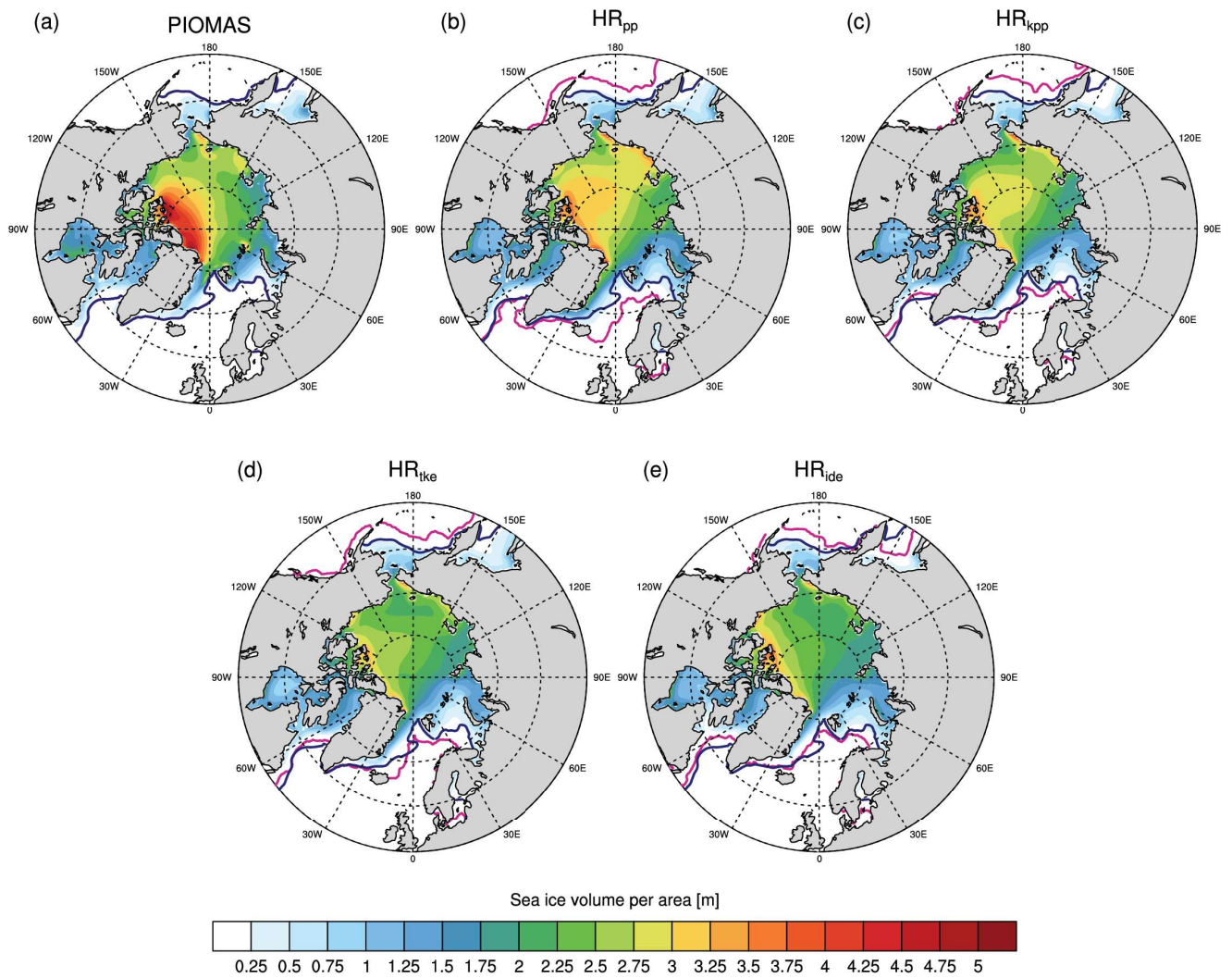


Figure 4. Time-averaged Arctic sea ice thickness in March for (a) PIOMAS reanalysis (March 1979–2005; Zhang and Rothrock, 2003; Schweiger et al., 2011), (b) HR_{pp} , (c) HR_{kpp} , (d) HR_{tke} , (e) HR_{ide} . The 15 % sea ice concentration of the EUMETSAT OSI SAF (averaged over March 1979–2005) is contoured in dark blue and those of the simulations in magenta.

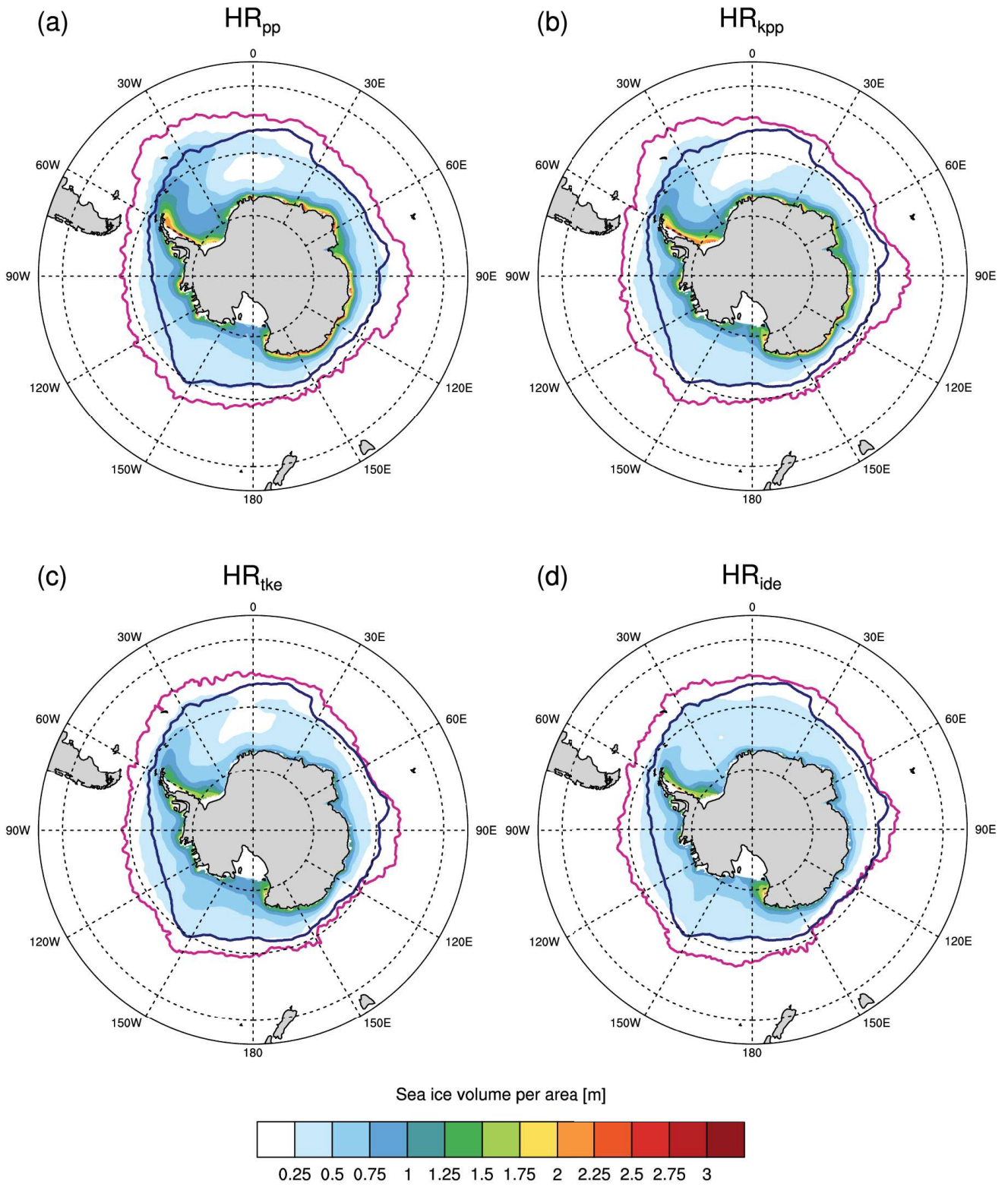


Figure 5. Time-averaged Arctic sea ice thickness in March for (a) HR_{pp} , (b) HR_{kpp} , (c) HR_{tke} , (d) HR_{ide} . The 15% sea ice concentration of the EUMETSAT OSI SAF (averaged over March 1979–2005) is contoured in dark blue and those of the simulations in magenta.

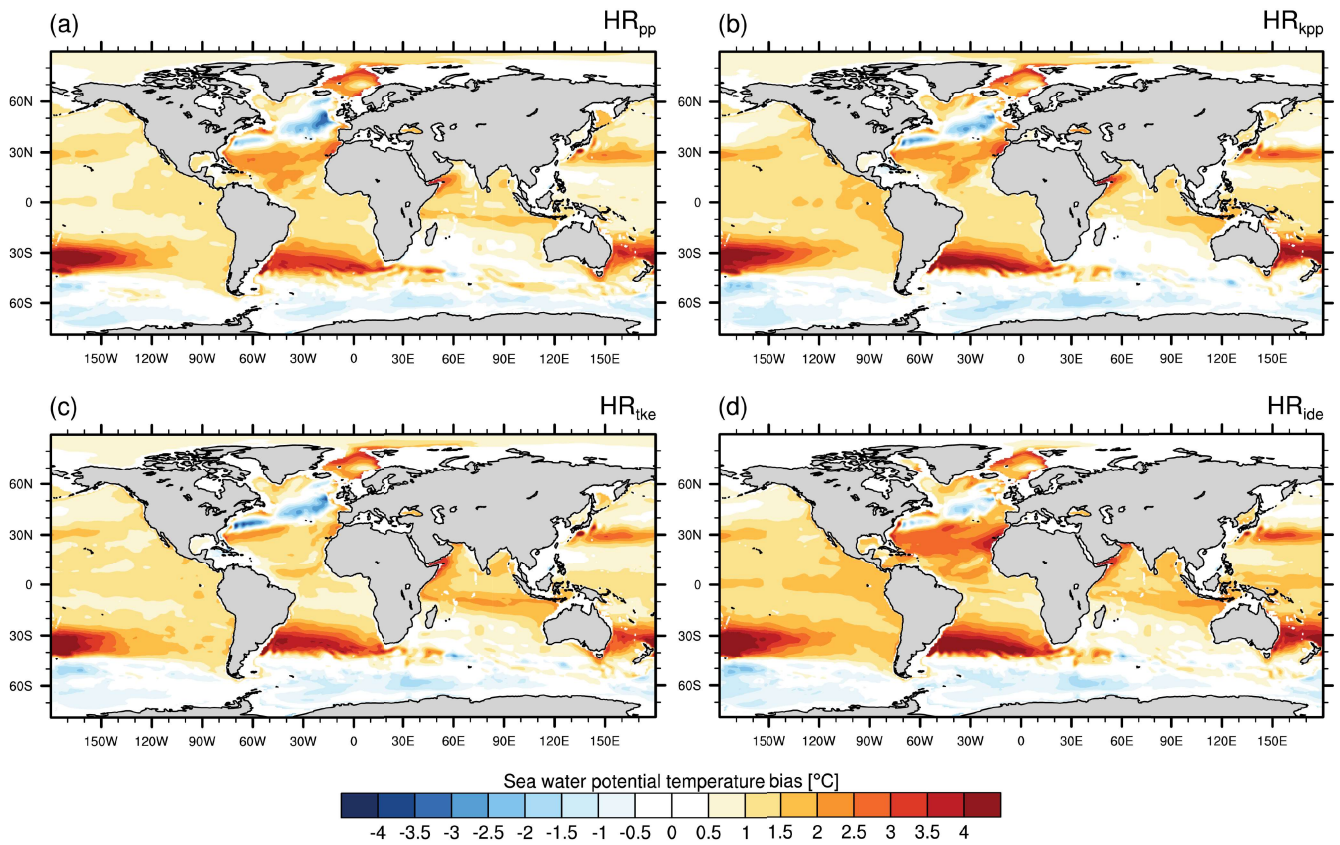


Figure 6. Time-averaged potential temperature bias of MPI-ESM1.2-HR minus EN4 (1945-1955) at a depth of 740 m for (a) HR_{pp} , (b) HR_{kpp} , (c) HR_{tke} , and (d) HR_{ide} .

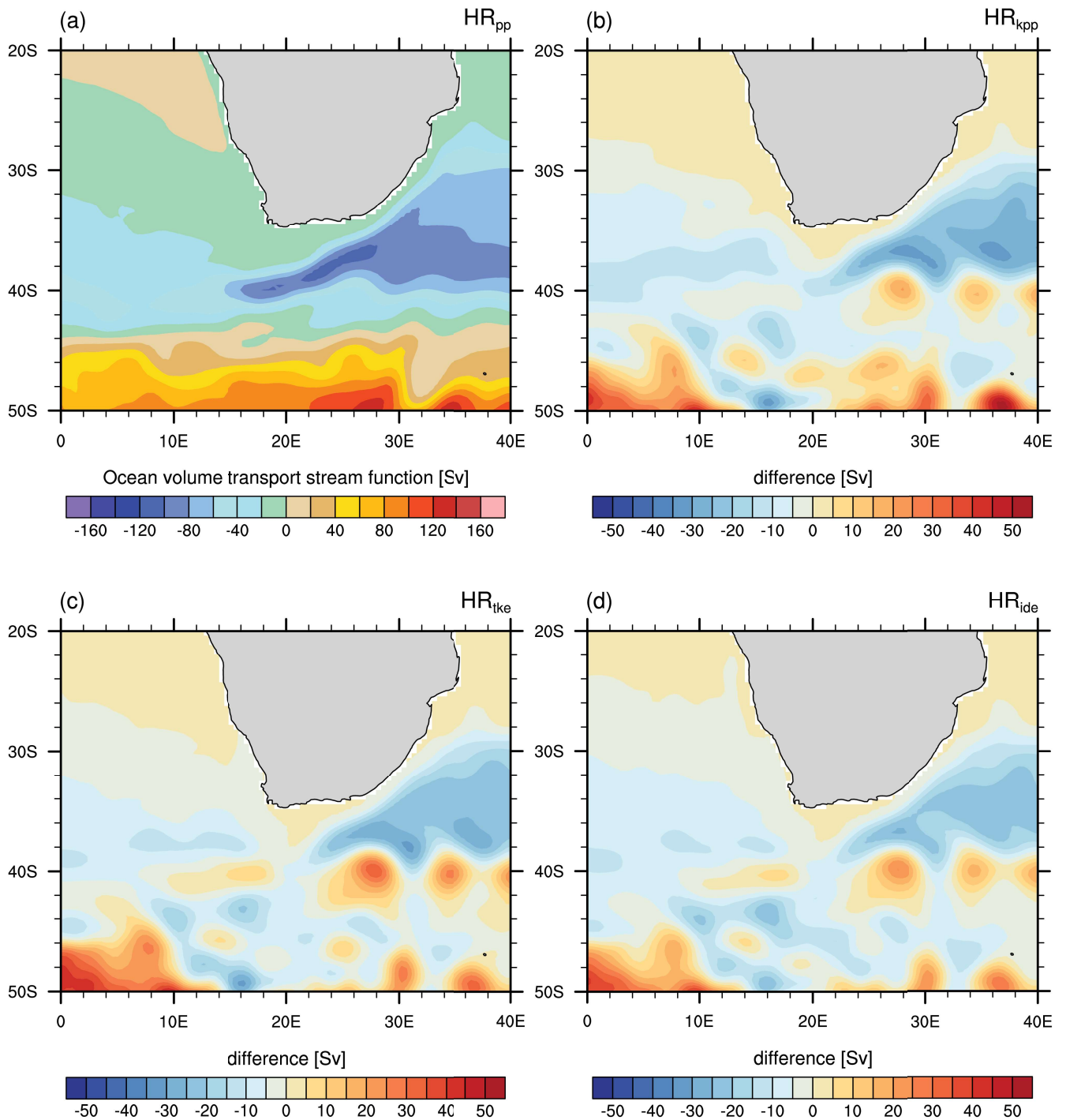


Figure 7. Time-averaged volume transport in the Agulhas region south of Africa as simulated by MPI-ESM1.2 (a) HR_{pp} and the difference (experiment minus HR_{pp}) for (b) HR_{kpp}, (c) HR_{tke}, and (d) HR_{ide}.

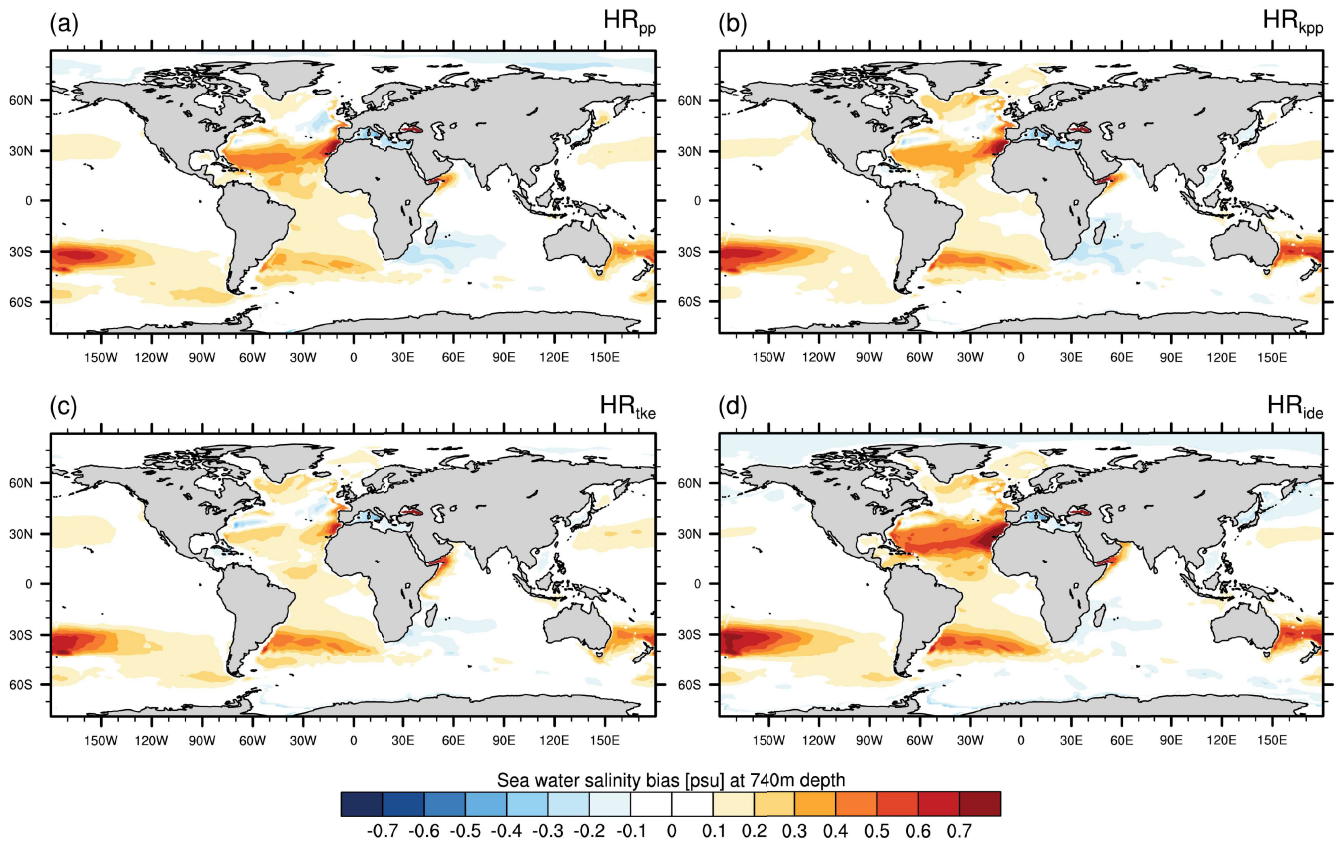


Figure 8. Time-averaged salinity bias of MPI-ESM1.2-HR minus EN4 (1945-1955) at a depth of 740 m for (a) HR_{pp} , (b) HR_{kpp} , (c) HR_{tke} , and (d) HR_{ide} .

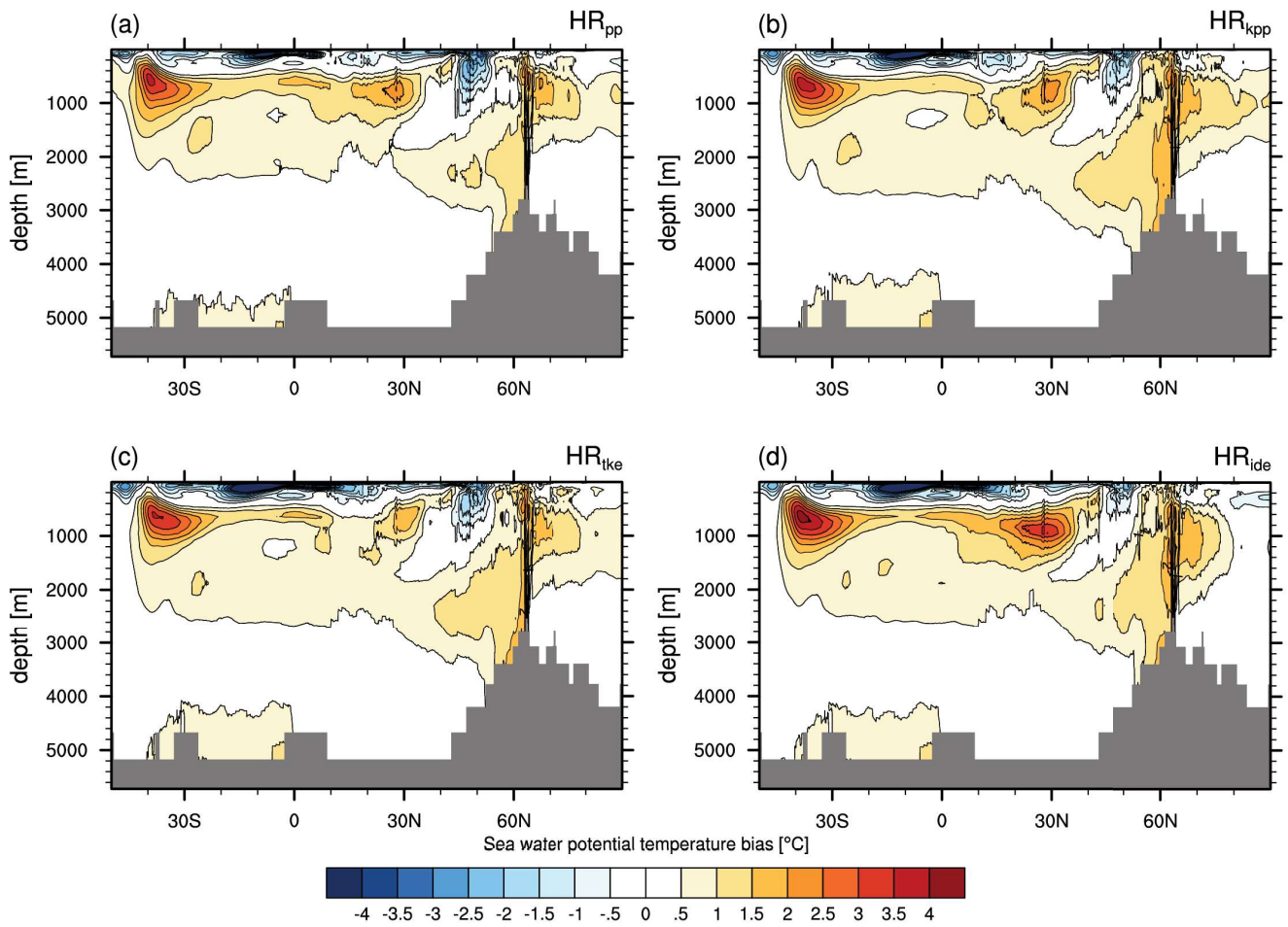


Figure 9. Zonal-mean potential temperature bias of MPI-ESM1.2-HR minus EN4 (1945-1955) in the Atlantic and Arctic Ocean for (a) HR_{pp} , (b) HR_{kpp} , (c) HR_{tke} , and (d) HR_{ide} .

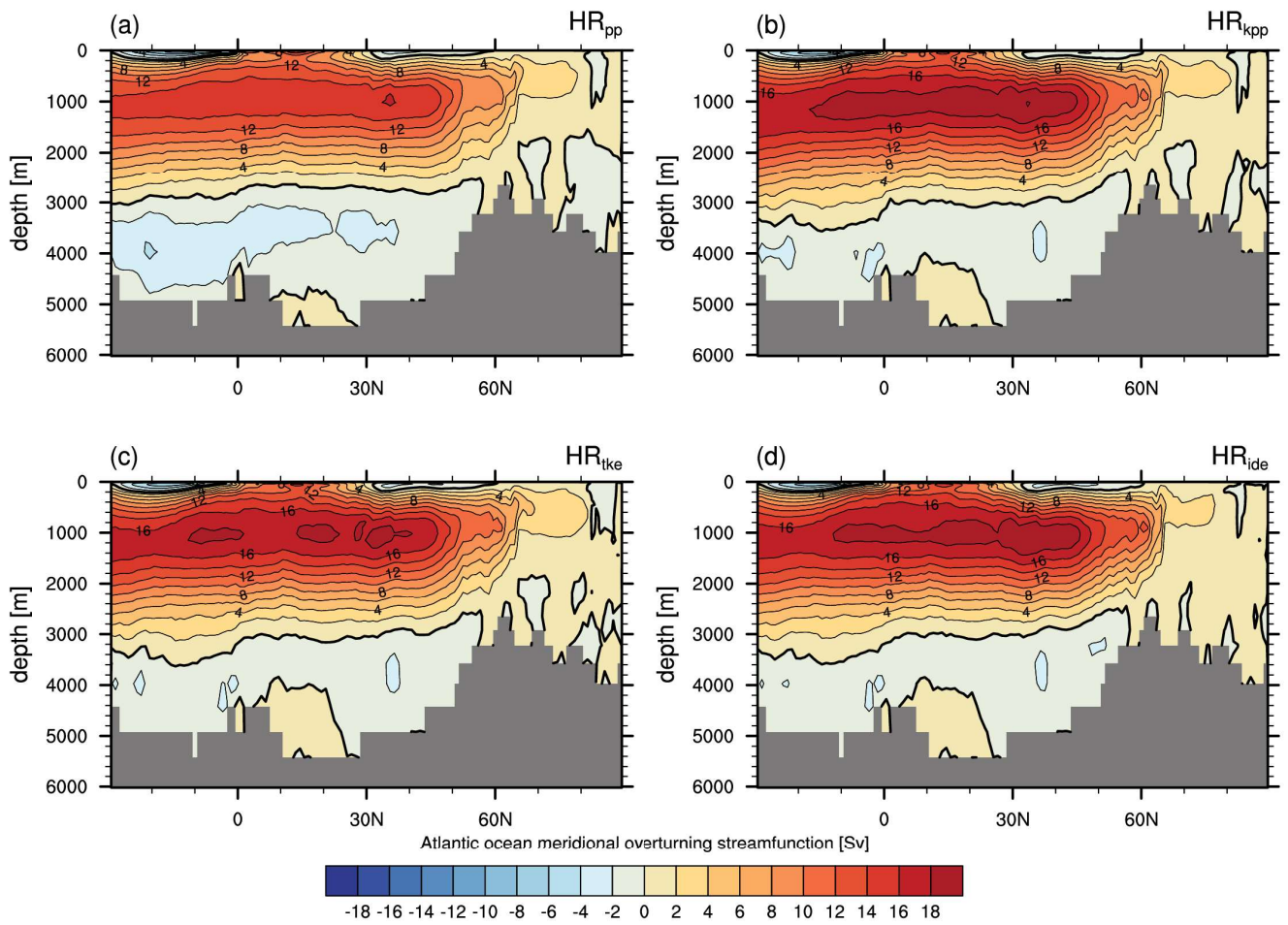


Figure 10. Eulerian stream function ($Sv = 10^6 \text{ m}^3 \text{ s}^{-1}$) of the AMOC in depth space simulated by MPI-ESM1.2 (a) HR_{pp} , (b) HR_{kpp} , (c) HR_{tke} , and (d) HR_{ide} .

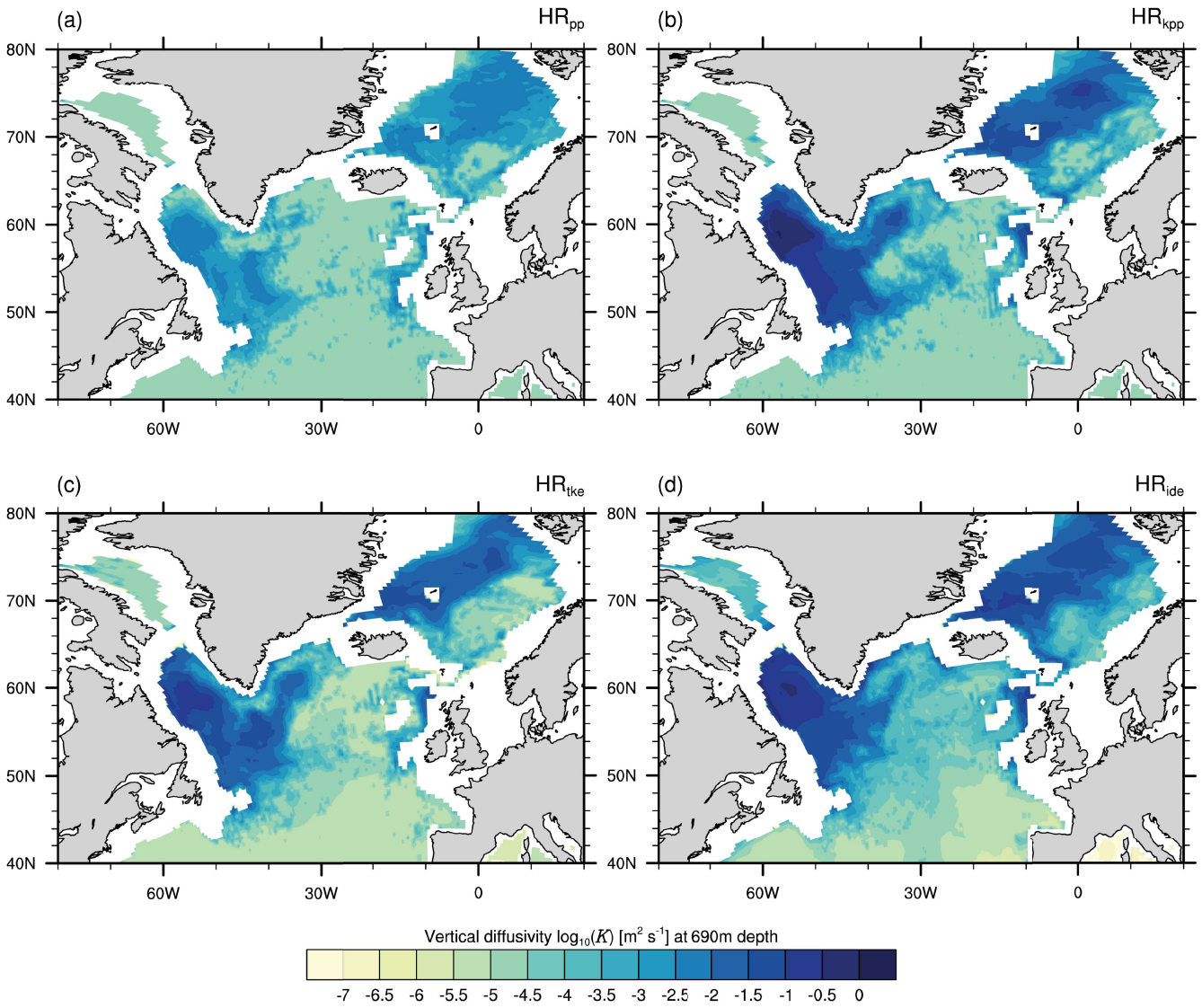


Figure 11. Time-averaged vertical diffusivity $\log_{10}(K)$ ($m^2 s^{-1}$) at a depth of 690m in the subpolar North Atlantic simulated by MPI-ESM1.2 (a) HR_{pp} , (b) HR_{kpp} , (c) HR_{tke} , and (d) HR_{idc} .

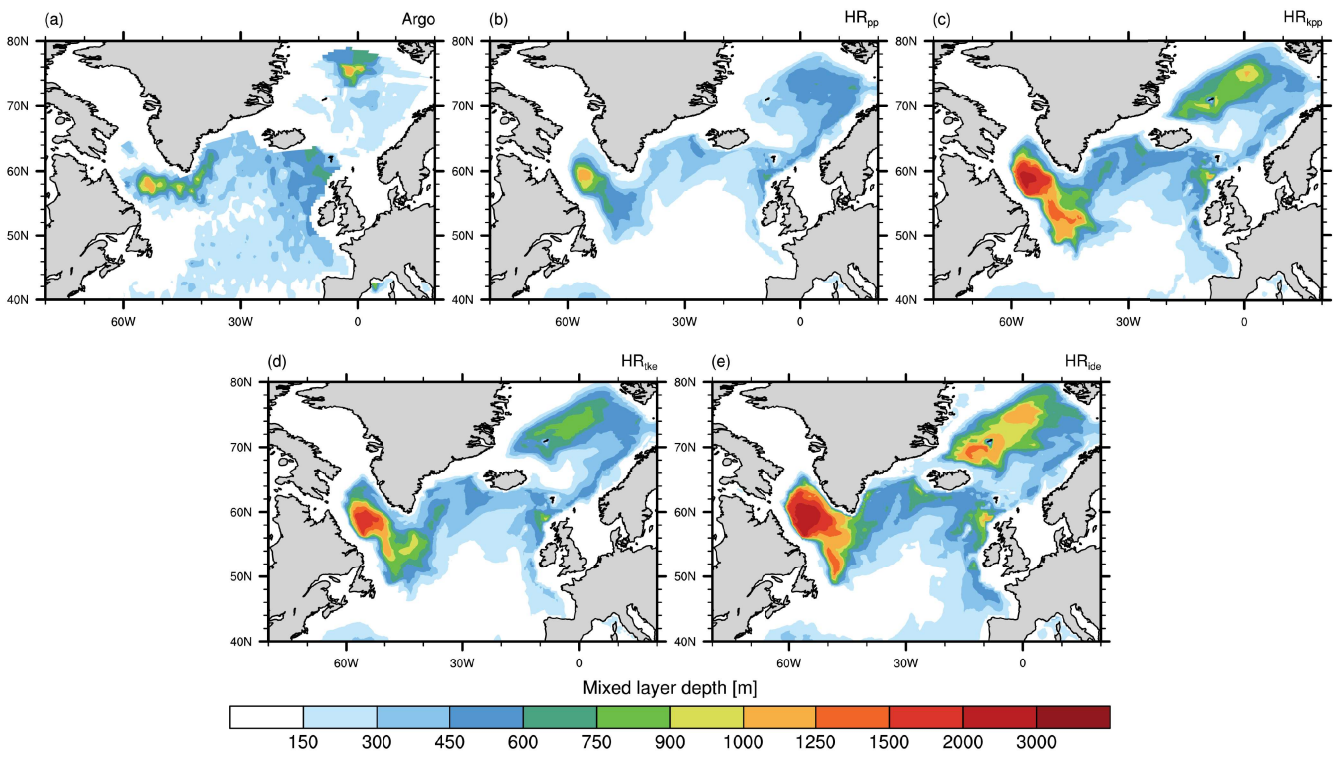


Figure 12. Time-averaged mixed layer depths (m) in March calculated by the density threshold method ($\sigma_t = 0.03 \text{ kg m}^{-3}$) from (a) $1^\circ \times 1^\circ$ Argo float data (Holte et al., 2017) (mean March from 2000 to 2018) and from MPI-ESM1.2 (b) HR_{pp} , (c) HR_{kpp} , (d) HR_{ike} , and (e) HR_{ide} .

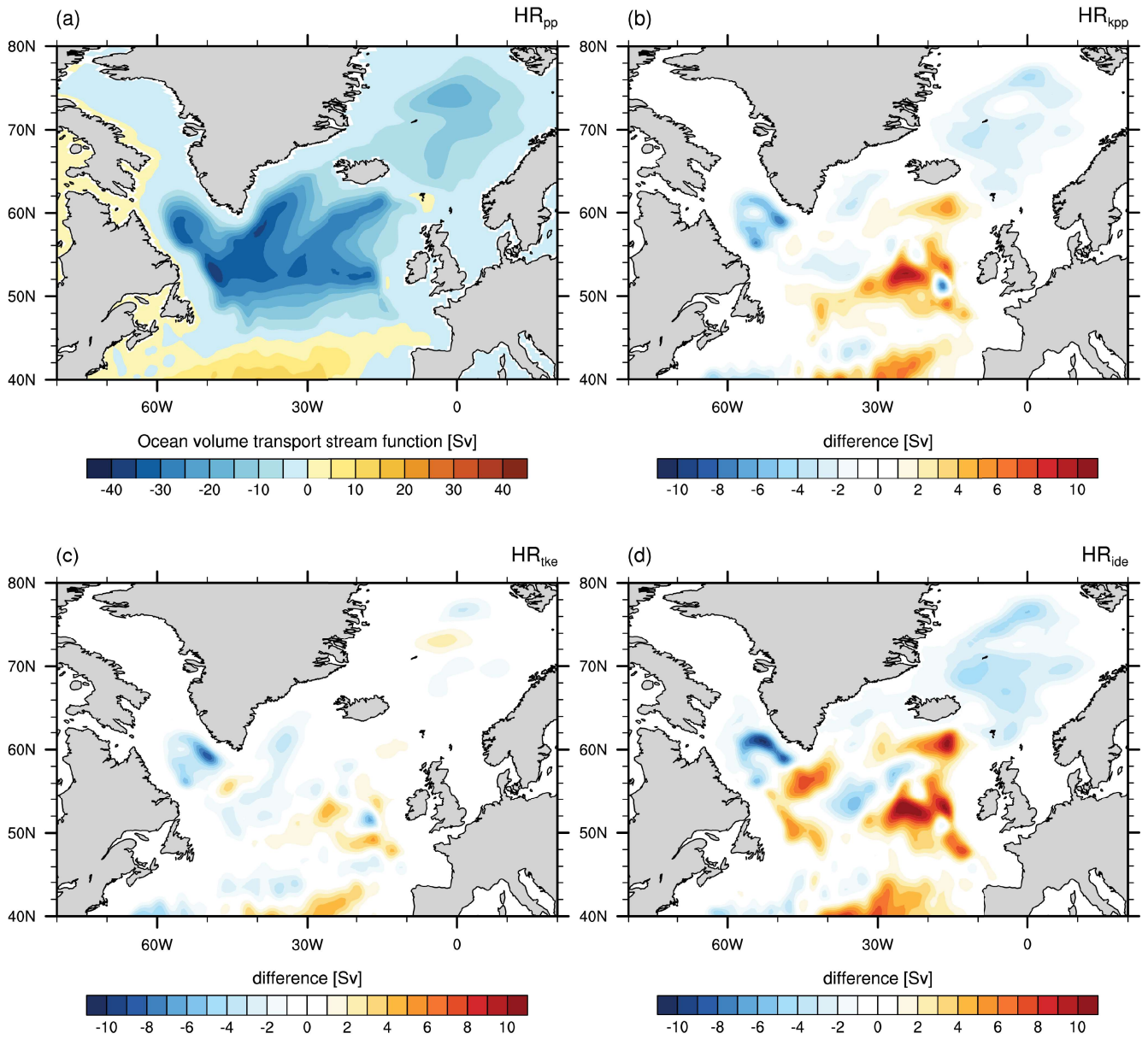


Figure 13. Time-averaged barotropic volume transport stream function (Sv) in the North Atlantic as simulated by MPI-ESM1.2 (a) HR_{pp}, and the differences "experiment - HR_{pp}" for (b) HR_{kpp}, (c) HR_{ike}, and (d) HR_{ide}.

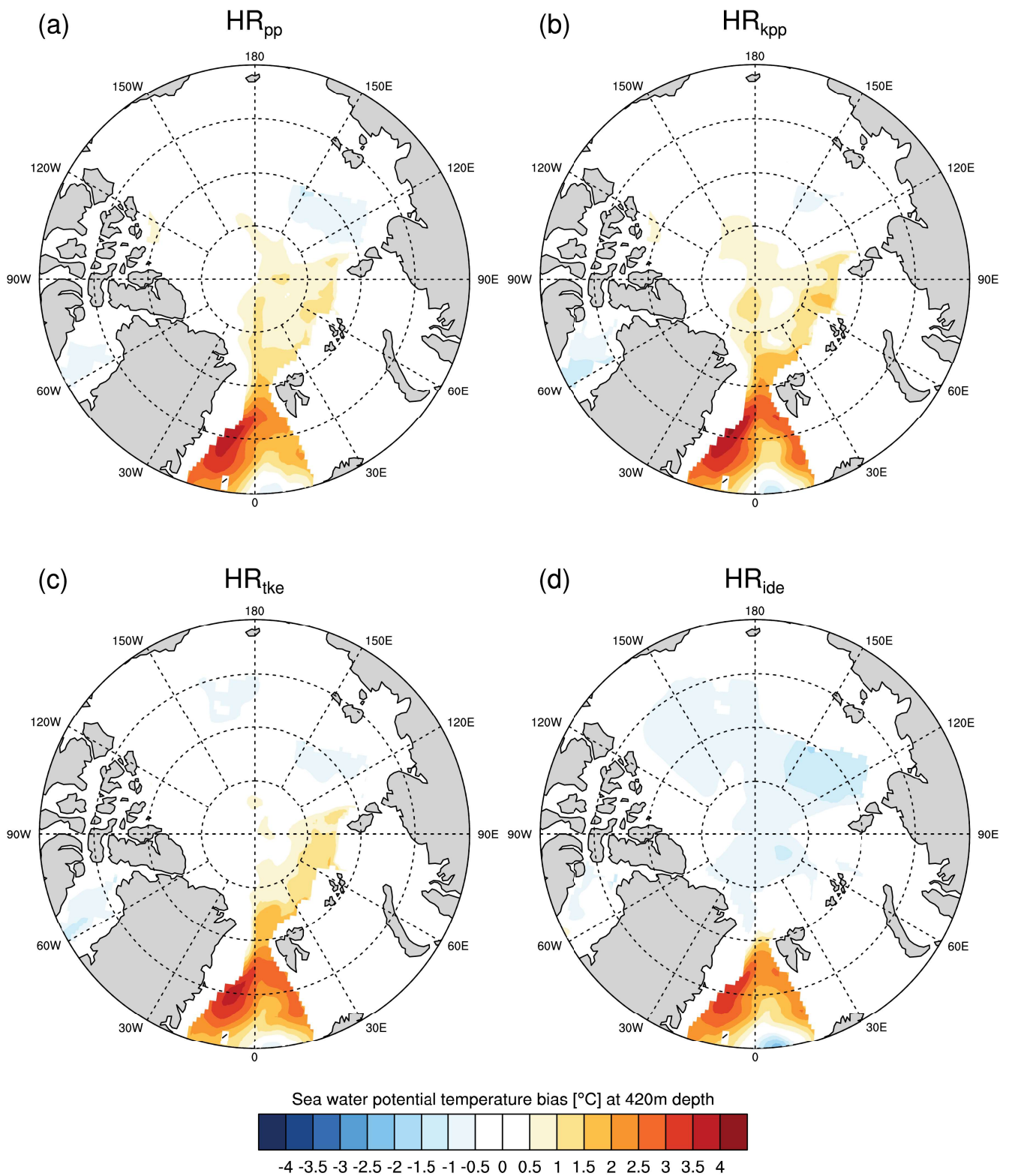


Figure 14. Time-averaged potential temperature bias of MPI-ESM1.46HR minus EN4 (1945-1955) at a depth of 420 m in the Arctic Ocean and at Fram Strait for (a) HR_{pp} , (b) HR_{kpp} , (c) HR_{tke} , and (d) HR_{ide} .

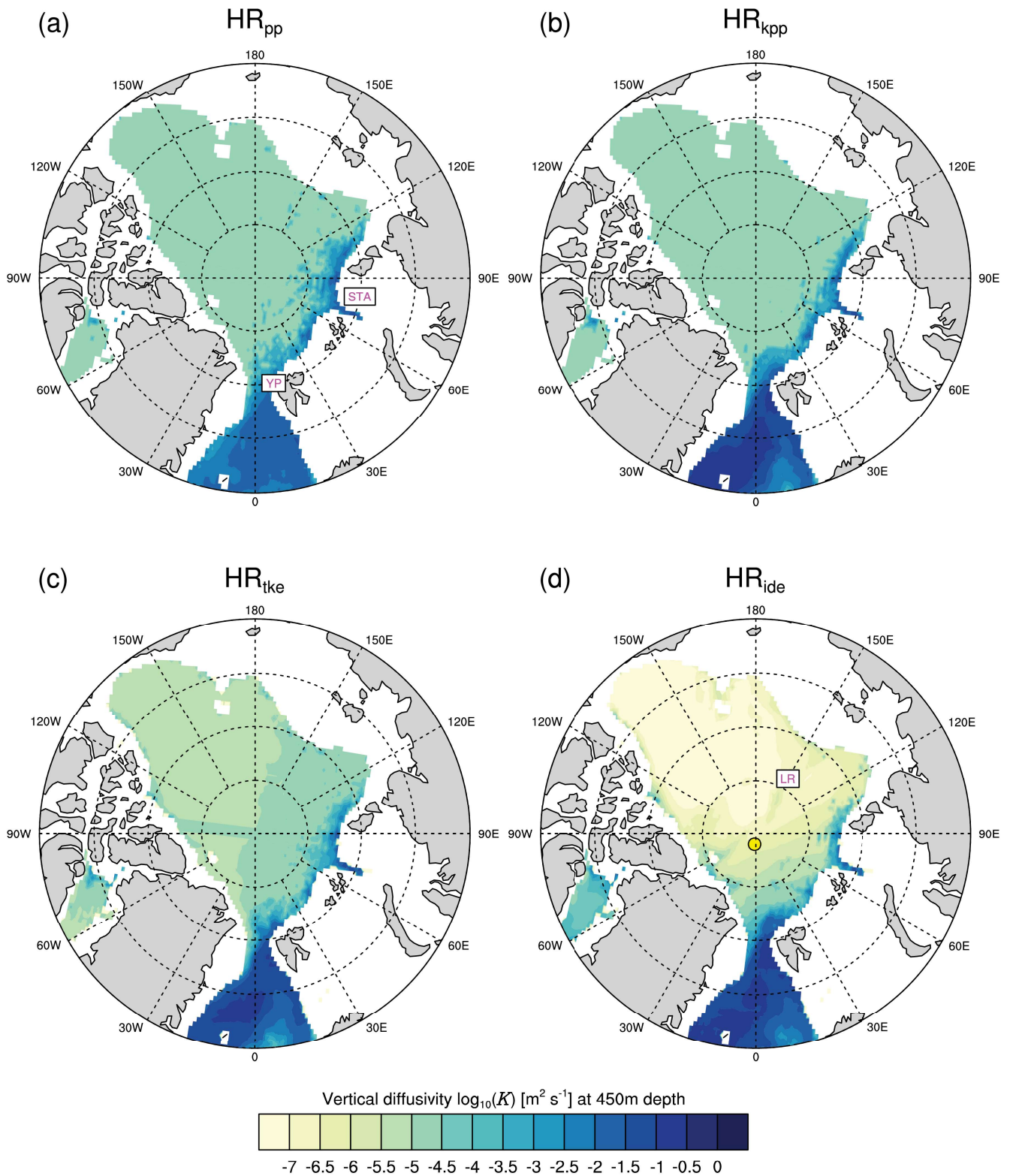


Figure 15. Time-averaged vertical diffusivity $\log_{10}(K)$ ($m^2 s^{-1}$) at depth of 450 m in the Arctic Ocean and at Fram Strait simulated by MPI-ESM1.2 (a) HR_{pp} , (b) HR_{kpp} , (c) HR_{tke} , and (d) HR_{ide} . YP: Yermak Plateau, STA: St. Anna Trough, LR: Lomonosov Ridge. The yellow point marks the approximate position ($7^\circ W$, $89^\circ N$) of the Barneo ice camp in the Amundsen Basin, where K on the $O(10^{-6} m^2 s^{-1})$ was

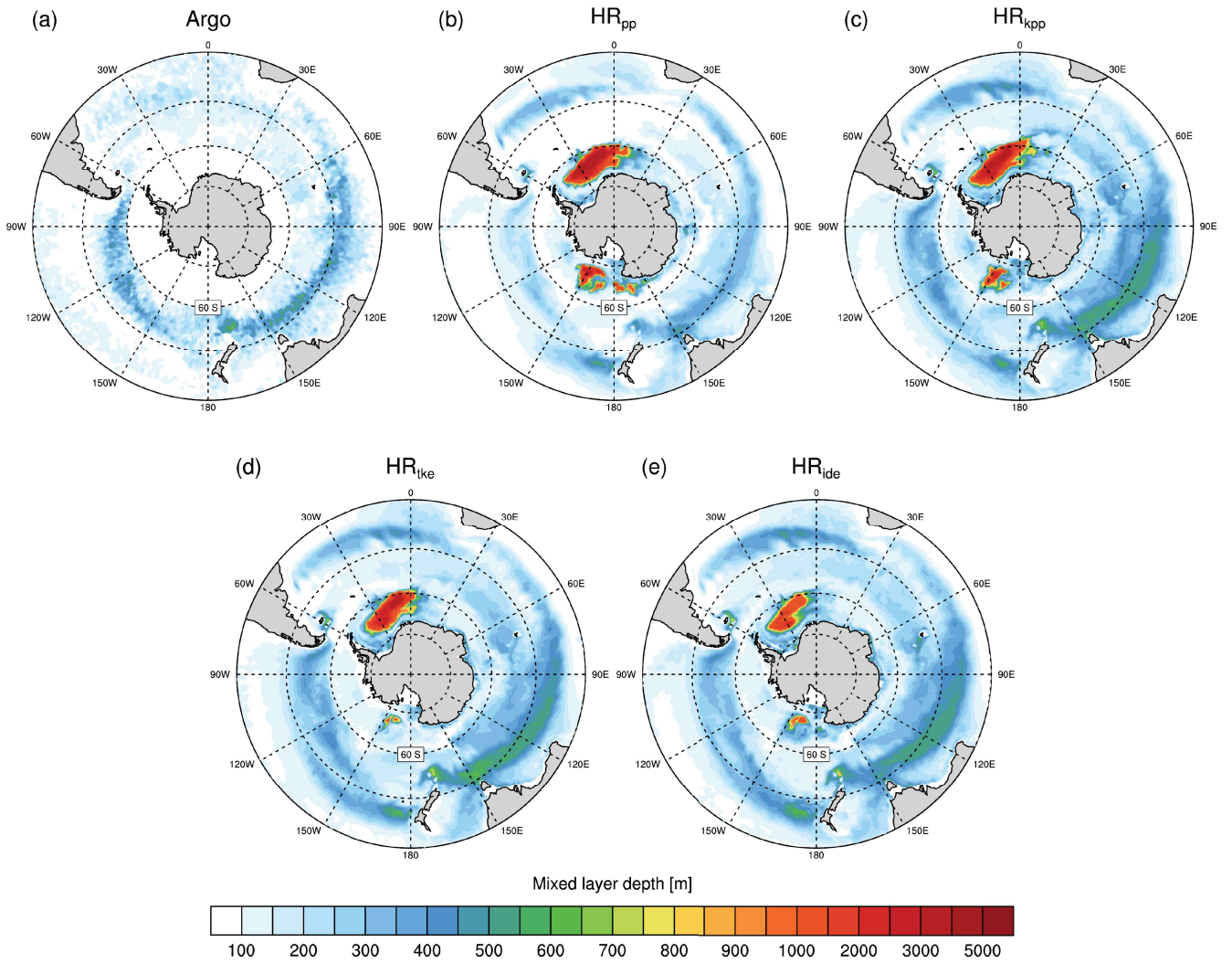


Figure 16. Time-averaged mixed layer depths (m) in September calculated (a) from $1^\circ \times 1^\circ$ Argo float data (Holte et al., 2017) (mean September from 2000 to 2018) by the density threshold method ($\sigma_t = 0.03 \text{ kg m}^{-3}$) and from MPI-ESM1.2 (b) HR_{pp} , (c) HR_{kpp} , (d) HR_{tke} , and (e) HR_{ide} . Note that there are no Argo data south of 60°S .

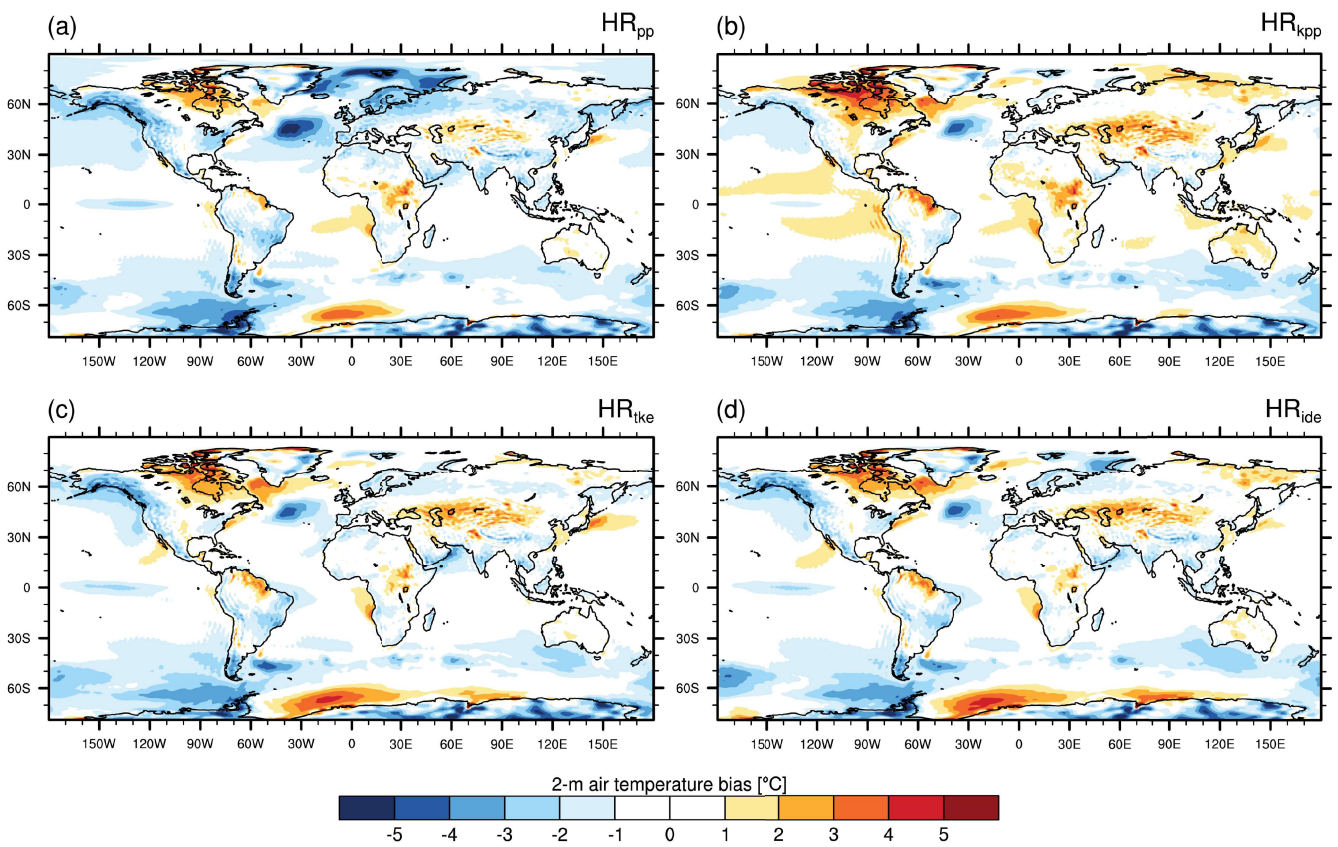


Figure 17. Time-averaged 2 m air temperature (SAT) bias (MPI-ESM1.2 minus EN4) for (a) HR_{pp}, (b) HR_{kpp}, (c) HR_{tke}, and (d) HR_{ide}.

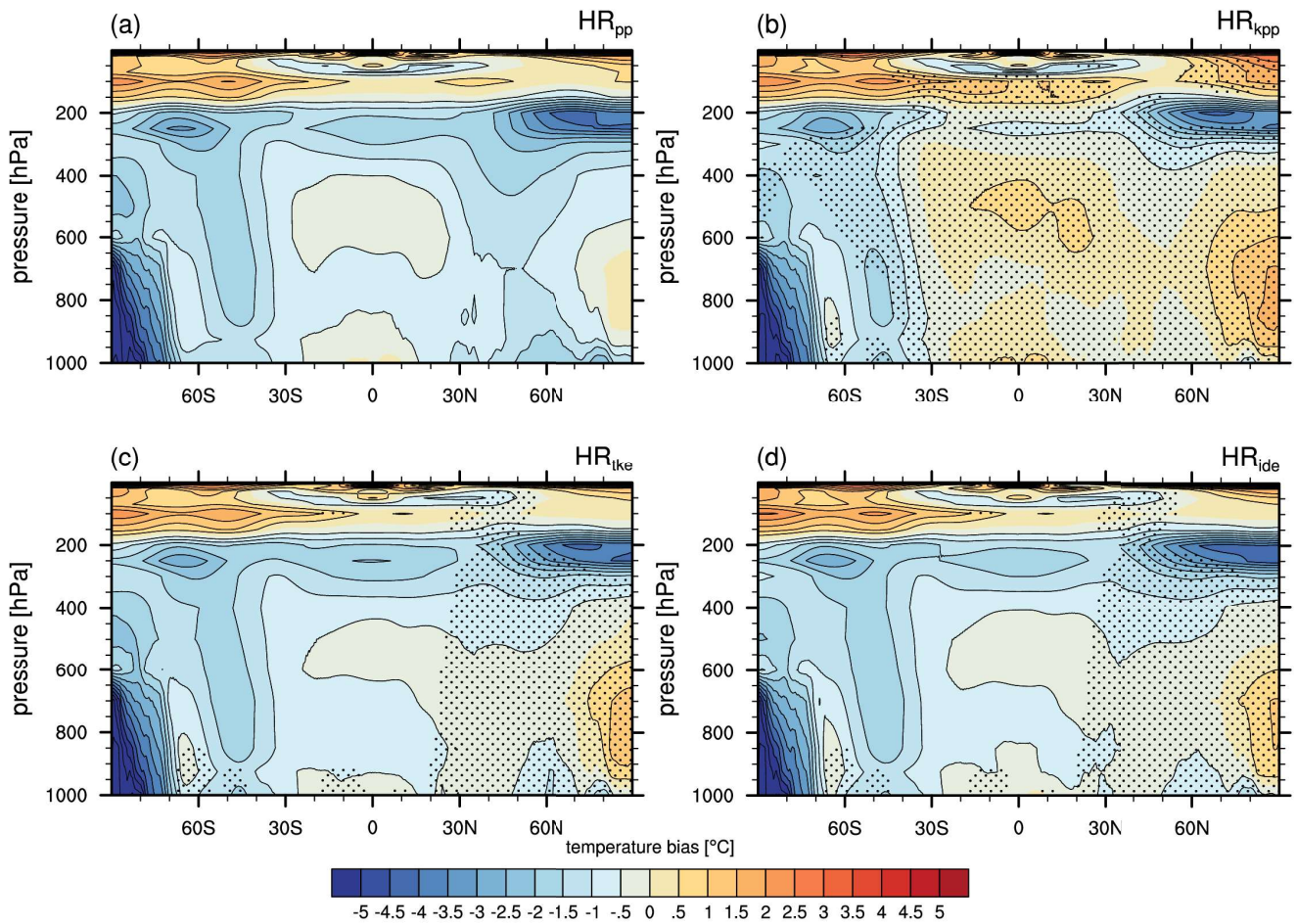


Figure 18. Time-averaged zonal air temperature bias (MPI-ESM1.2 minus EN4) for (a) HR_{pp} , (b) HR_{kpp} , (c) HR_{tke} , and (d) HR_{ide} . Stippling in (a-c) shows where the difference to HR_{pp} is significant at $\alpha = 5\%$ based on adjusted p-values with the FDR method (Benjamini and Hochberg, 1995) using $\alpha_{FDR} = 5\%$ to account for multiplicity.

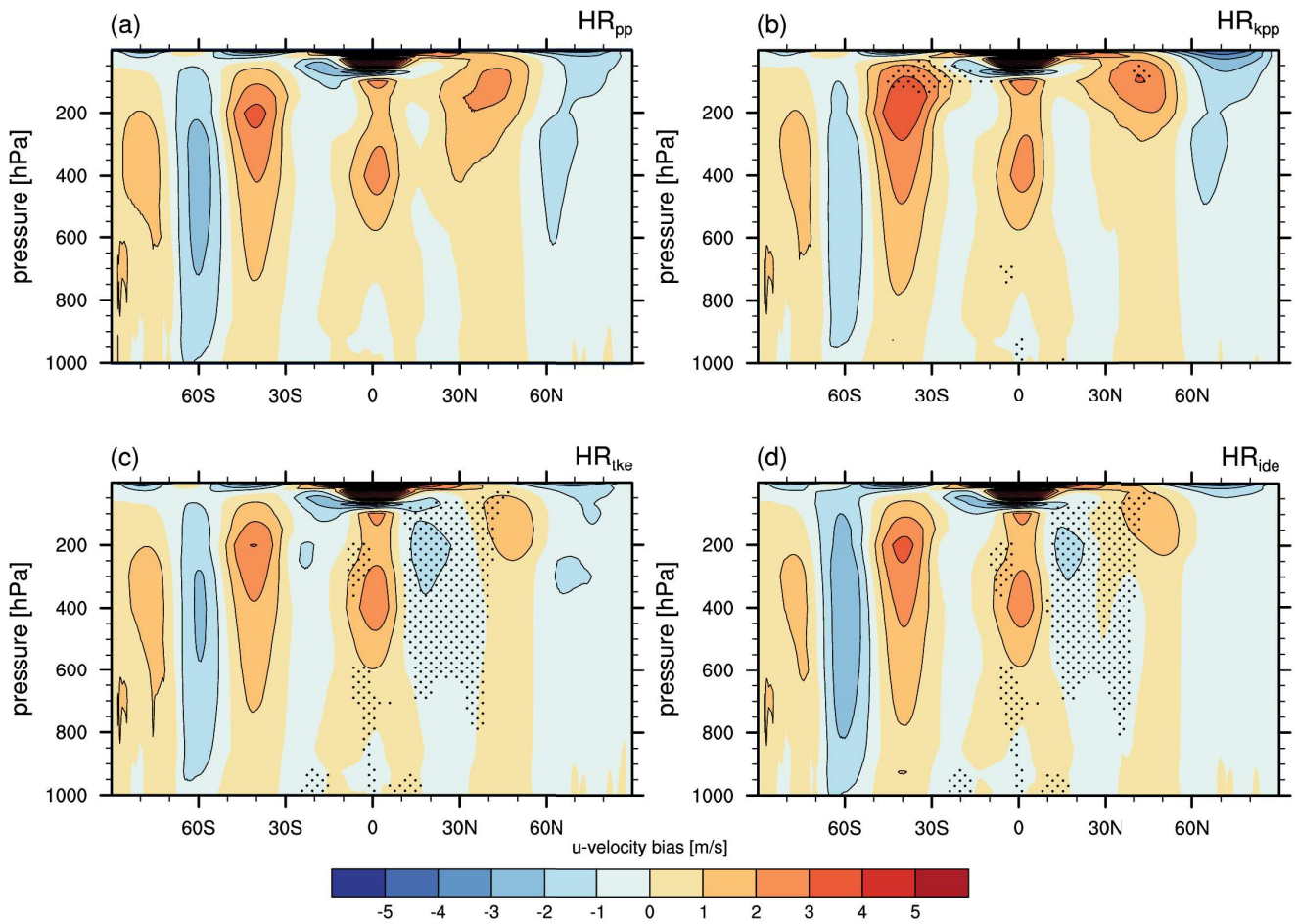


Figure 19. Time-averaged zonal wind speed bias (MPI-ESM1.2 minus EN4) for (a) HR_{pp}, (b) HR_{kpp}, (c) HR_{ike}, and (d) HR_{ide}. Stippling in (a-c) shows where the difference to HR_{pp} is significant at $\alpha = 5\%$ based on adjusted p-values with the FDR method (Benjamini and Hochberg, 1995) using $\alpha_{FDR} = 5\%$ to account for multiplicity.

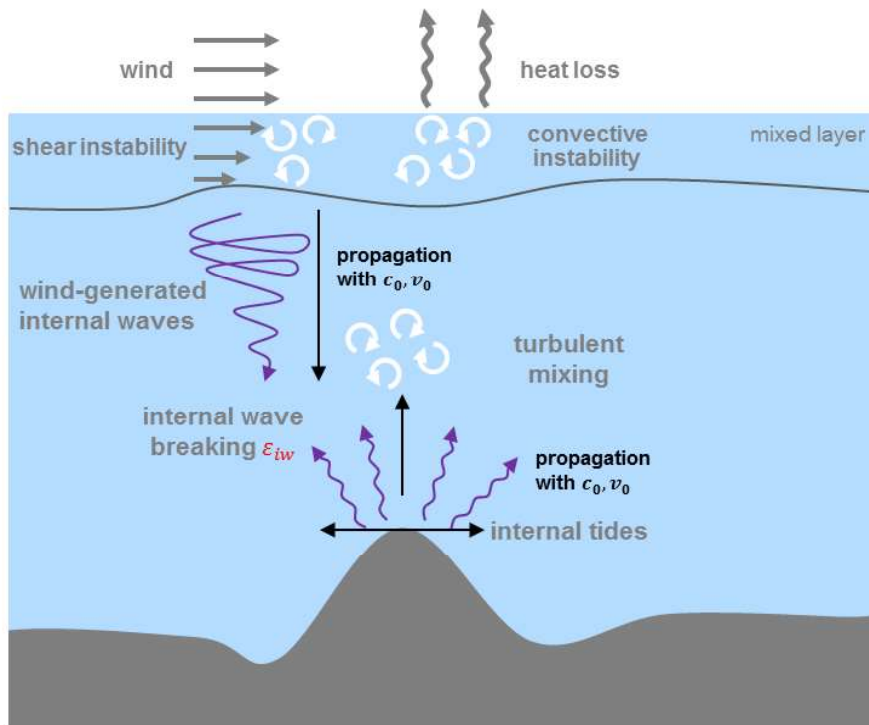


Figure A1. Schematic of the combined TKE+IDEMIX scheme used in HR_{ide} . Processes parameterised in TKE: away from strong currents, shear and buoyancy instability (convection) is largest near the surface (grey arrows), causing strong mixing in the mixed layer (white eddy symbols). Processes parameterized by IDEMIX: below the mixed layer, internal waves are either induced by fluctuating wind stress or by interactions of barotropic tides with orographic features (violet arrows). The internal waves are propagating into the interior ocean (black arrows), where they eventually break and dissipate (white eddy symbols).

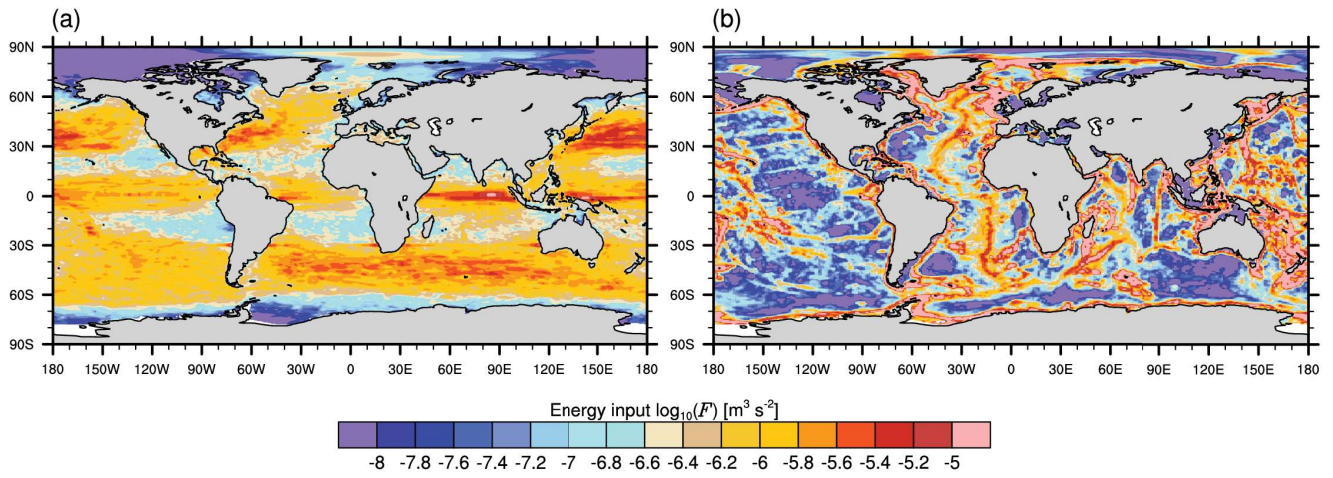


Figure A2. Energy input $\log_{10}(F)$ ($\text{m}^3 \text{s}^{-3}$) at (a) the surface by near-inertial waves from Rimac et al. (2013) and (b) by tidal forcing at the ocean bottom from Jayne (2009).

Table A1. Resulting p -values from Welch's two-sided t -tests ($\alpha = 0.05$ and $n = 20$) for testing the differences in mean overflow volumes of Denmark Strait overflow (DSOW), in the Faroe-Shetland Channel (FSC), and in the Faroe Bank Channel (FBC).

	Experiment	HR _{pp}	HR _{kpp}	HR _{tke}	HR _{ide}
DSOW	HR _{pp}	-	0.0*	0.0*	0.0*
	HR _{kpp}	-	-	0.48	0.52
	HR _{tke}	-	-	-	0.13
	HR _{ide}	-	-	-	-
FSC	HR _{pp}	-	0.23	0.0*	0.52
	HR _{kpp}	-	-	0.02*	0.50
	HR _{tke}	-	-	-	0.0*
	HR _{ide}	-	-	-	-
FBC	HR _{pp}	-	0.72	0.0*	0.0*
	HR _{kpp}	-	-	0.0*	0.01*
	HR _{tke}	-	-	-	0.0*
	HR _{ide}	-	-	-	-

To achieve a power $(1-\beta)$ of 80% with $n = 20$ and $\alpha = 0.05$, the minimum effect size $d = |\mu_1 - \mu_2| / \sqrt{(sd_1^2 + sd_2^2)/2}$ is about 1.0. For instance, a pooled standard deviation of e.g. 0.1 Sv would correspond to a minimum mean difference of $|\mu_1 - \mu_2| = 0.1 \text{ Sv}$.